Generalization of the k·p approach for strained layered semiconductor structures grown on high-index-planes

J. Los and A. Fasolino
Istituto Nazionale per la Fisica della Materia, Dipartimento di Fisica, Università di Modena, Via Campi 213/A, 41100 Modena, Italy

A. Catellani
Istituto di Materiale Speciali per Elettronica, CNR, Via Chiavari, 18/A, 43100 Parma, Italy
(Received 18 August 1995)

We present a generalized theoretical description of the 8×8 $\mathbf{k}\cdot\mathbf{p}$ approach for determining the band structure of layered semiconductor structures for any growth direction, including strain and piezoelectric effects. The definition of heavy, light, and splitoff hole states is extended to arbitrary growth directions in analogy to the conventional (001) case, by choosing an adapted set of basis functions. The choice of this basis allows a qualitative understanding of the in-plane band structure and of the optical properties of strained and unstrained structures. Besides, we solve the $\mathbf{k}\cdot\mathbf{p}$ Hamiltonian by means of an efficient real-space method allowing us to deal with arbitrary confining potentials. The theory is applied to unstrained, compressively strained, and tensilely strained quantum wells. We find that confinement energies, warping, and in-plane effective masses strongly depend on the direction of confinement and on strain. Piezoelectric effects further affect the dispersion for all growth directions other than (001) and (011). We also find that the optical transition strength depends on the in-plane light polarization for growth directions other than (001) and (111).

I. INTRODUCTION

Since the advent of molecular-beam epitaxy (MBE), semiconductor material engineering has become a topic of great technological and fundamental interest. Initial work concentrated on the effects of size quantization, dominated by the conduction band, but, later, it was shown that valence band engineering by use of strained layers[1–3] could drastically affect and improve all optical properties (lasers, LED's) and provide good *p*-type electronic components for complementary electronics.

Another possibility, realized more recently, for tuning the electronic and optical properties is offered by the growth of epitaxial layers on high-index planes [i.e., other than (001)]. The interest of non-(001)-oriented semiconductor structures is manyfold, concerning growth and impurities incorporation,[4] self-organized growth,[5] electronic properties,[6,7] and lasing performances.[7–9] Here, we will focus on the electronic and optical properties of semiconductor quantum well (QW) structures grown on novel index planes, also in the presence of strain.

On the experimental side there have been many reports of successful high-quality growth of (11N)-oriented unstrained $GaAs/Al_xGa_{1-x}As$ QW structures as evidenced by their surface morphology, good optical properties, and high electron and hole gas mobilities.[10–17] An extremely high hole gas mobility was observed in (113)-grown $GaAs/Al_xGa_{1-x}As$ QW structures.[4] The threshold current density of (111)-oriented QW's was found to be less than that of (001)-oriented ones.[9] Good optical properties are also reported for compressively strained (111)-oriented $In_xGa_{1-x}As/Al_yGa_{1-y}As$ QW structures.[18]

The starting point for our theoretical investigations is the $\mathbf{k}\cdot\mathbf{p}$ approach, which has been developed by Luttinger and Kohn[19] to deal with the problem of an electron moving in a perturbed periodic structure and put forward for the use in QW structures by White and Sham[20] and by Bastard.[21] Within this theory, a number of studies concerning non-(001)-oriented QW's appeared in the literature[6–8,22,23] [Refs. 6 and 7 for (11N)-, Refs. 8 and 23 for (111)-, and Ref. 22 for (113)-grown QW's], but no comprehensive treatment for a generic (hkl) growth direction exists to our knowledge. In particular, little has been done for non-(001)-oriented strained QW structures, where strong piezoelectric fields occur.[24]

In Sec. II we (i) generalize the $\mathbf{k}\cdot\mathbf{p}$ treatment to deal with a generic (hkl) growth direction extending the definition of heavy hole (hh), light hole (lh), and splitoff (so) states by choosing a symmetry-adapted set of basis functions, (ii) give a complete description of how to deal with strain and piezoelectricity, and (iii) present an efficient numerical method of solution of the multiband Hamiltonian based on a real-space discretized description of the wave function and capable of dealing with arbitrary confining potentials, and those due to piezoelectric fields. In Sec. III we present numerical results for unstrained $GaAs/Al_xGa_{1-x}As$, compressively strained $In_xGa_{1-x}As/Al_yGa_{1-y}As$ and tensilely strained $GaP_xAs_{1-x}/Al_yGa_{1-y}As$ QW's. We show that the in-plane band structure and the optical properties can be qualitatively very well understood in terms of the generalized hh, lh, and so states and of the corresponding effective masses in perpendicular direction. A particularly interesting observation is the dependence of light absorption on the linear in-plane polarization for low symmetry growth directions, in contrast to the behavior of (001)-grown QW structures. Finally, we give a conclusive summary in Sec. IV.

II. FORMALISM AND SOLUTION METHOD

The description of the formalism is divided into four steps. First, in Sec. II A we formulate the $\mathbf{k}\cdot\mathbf{p}$ approach in a

form which is independent of the growth direction, next, in Sec. II B we extend the definition of heavy, light, and splitoff hole states, and the ensuing selection rules for optical transitions by introducing a growth direction adapted set of basis functions. The additional effects due to strain and piezoelectricity are examined in Sec. II C and, finally, in Sec. II D we describe an advantageous numerical method of solution of the multiband Hamiltonian problem.

A. k·p Hamiltonian

In the eight-band Kane model[25] of the **k·p** theory approach for II-VI, III-V, and group IV semiconductor bulk materials the lowest conduction band states and the upper valence band states at wave vectors **k** near the Γ point are expanded in terms of the eight zone center eigenstates composed of the spatial $L=0$ conduction band basis function $|S\rangle$ and of the $L=1$ valence band basis functions $|X\rangle$, $|Y\rangle$, and $|Z\rangle$ plus spin. The spin-orbit coupling splits the sixfold degenerate valence band states into the fourfold degenerate $J=3/2$ states (Γ_8 symmetry) at energy E_v and the twofold degenerate $J=1/2$ splitoff states (Γ_7 symmetry) at energy $E_{\rm so}=E_v-\Delta_{\rm so}$, where $\Delta_{\rm so}$ is the spin-orbit energy splitting. The conduction band edge (at $\mathbf{k}=0$) is located at $E_c=E_v+E_g$, where E_g is the energy gap. We choose the eight basis functions as follows:

$$
\begin{aligned}
u_1(\mathbf{r})&=u_{c\uparrow}(\mathbf{r})=|S\uparrow\rangle,\\
u_2(\mathbf{r})&=u_{c\downarrow}(\mathbf{r})=|iS\downarrow\rangle,\\
u_3(\mathbf{r})&=|3/2,+3/2\rangle=u_{\rm hh\uparrow}(\mathbf{r})=\sqrt{1/2}|X+iY\uparrow\rangle,\\
u_4(\mathbf{r})&=|3/2,-3/2\rangle=u_{\rm hh\downarrow}(\mathbf{r})=i\sqrt{1/2}|X-iY\downarrow\rangle,\\
u_5(\mathbf{r})&=|3/2,+1/2\rangle=u_{\rm lh\uparrow}(\mathbf{r})\\
&=i\sqrt{1/6}|X+iY\downarrow\rangle-i\sqrt{2/3}|Z\uparrow\rangle,\\
u_6(\mathbf{r})&=|3/2,-1/2\rangle\\
&=u_{\rm lh\downarrow}(\mathbf{r})=\sqrt{1/6}|X-iY\uparrow\rangle+\sqrt{2/3}|Z\downarrow\rangle,\\
u_7(\mathbf{r})&=|1/2,+1/2\rangle=u_{\rm so\uparrow}(\mathbf{r})\\
&=\sqrt{1/3}|X+iY\downarrow\rangle+\sqrt{1/3}|Z\uparrow\rangle,\\
u_8(\mathbf{r})&=|1/2,-1/2\rangle=u_{\rm so\downarrow}(\mathbf{r})\\
&=-i\sqrt{1/3}|X-iY\uparrow\rangle+i\sqrt{1/3}|Z\downarrow\rangle,
\end{aligned}
\tag{1}
$$

where c, hh, lh, and so indicate the conduction and the heavy, light, and splitoff hole states, respectively. The interaction with all other bands, away from the band gap, is taken into account perturbatively.

In adapting the **k·p** approach to a layered structure, where the periodicity in the growth direction (e.g., the z' direction) is lost, the eigenstates at in-plane wave vector $\mathbf{k}'_\parallel$ are written as

$$
\begin{aligned}
\psi(\mathbf{r}')&=\sum_{i=1}^{8} e^{i\mathbf{k}'_\parallel\mathbf{r}'_\parallel}\phi_i(z')u_i(\mathbf{r}')\\
&=e^{i\mathbf{k}'_\parallel\mathbf{r}'_\parallel}\vec{\phi}(z')\cdot\vec{u}(\mathbf{r}'),
\end{aligned}
\tag{2}
$$

where the components of $\vec{\phi}(z')$, $\phi_1(z')\cdots\phi_8(z')$, are the envelope functions (replacing the plane wave $e^{ik'_z z'}$), the components of $\vec{u}(\mathbf{r}')$ are the Bloch basis function (1), and where we have used the approximation that these basis functions are the same for each layer. The eigenstates satisfy

$$
H_K(z')\vec{\phi}(z')=E\vec{\phi}(z'),
\tag{3}
$$

where $H_K(z')$ is the 8×8 **k·p** Hamiltonian which we write in the following general form:

$$
\begin{aligned}
H_K(z')=&\sum_{\alpha,\beta=x',y',z'} k'_\alpha D^{\alpha\beta}(z')k'_\beta+\sum_{\alpha=x',y',z'} F^\alpha k'_\alpha\\
&+V(z'),
\end{aligned}
\tag{4}
$$

where z' is the coordinate in the growth direction, $k'_z=-i\,d/dz'$ and where $D^{\alpha\beta}(z')=D^{\beta\alpha}(z')$ and F^α are 8×8 Hermitian matrices, which depend on the crystallographic growth direction. The diagonal matrix $V(z')=\mathrm{diag}[E_c(z'),E_c(z'),E_v(z'),E_v(z'),E_v(z'),E_v(z'),E_{\rm so}(z'),E_{\rm so}(z')]$ describes the potential profile in the z' direction with discontinuities at the interfaces due to the valence band offset and to the different E_g and $\Delta_{\rm so}$ of adjacent layer materials. We use primed indices for the coordinates to indicate that these are the coordinates relative to a basis which is rotated with respect to the usual simple cubic basis such that z' and k'_z are the coordinates in the growth direction (h,k,l). We have that $\mathbf{r}'=R\,\mathbf{r}$ and $\mathbf{k}'=R\,\mathbf{k}$, where R is an orthogonal transformation matrix, which we choose as

$$
R=\begin{bmatrix} c_1lh & c_1lk & -c_1(h^2+k^2)\\ -c_2k & c_2h & 0\\ c_3h & c_3k & c_3l \end{bmatrix},
\tag{5}
$$

where $c_1=1/\sqrt{l^2h^2+l^2k^2+(h^2+k^2)^2}$, $c_2=1/\sqrt{h^2+k^2}$, and $c_3=1/\sqrt{h^2+k^2+l^2}$ are normalization constants. With this choice the in-plane k'_x and k'_y directions are $(lh,lk,-h^2-k^2)$ and $(-k,h,0)$, respectively. Apart from the growth direction, the matrices $D^{\alpha\beta}(z')$ depend on the conduction band effective mass m_c^* and on the effective masses at the valence band edges, expressed in terms of the Luttinger parameters γ_1, γ_2, and γ_3. The matrices F^α describe the coupling between conduction and valence band states and depend on the p-matrix element $P=\langle S|p_x|X\rangle=\langle S|p_y|Y\rangle=\langle S|p_z|Z\rangle$. In Appendix A, H_K is given explicitly for the most studied case that z' is along the (001) direction of the simple cubic cell.

The Luttinger parameters are, in general, different for each layer and therefore depend on z'. The p-matrix element P is, however, independent of the layer as a consequence of the assumption that the basis functions (1) are equal for each layer. In this approximation, the matrices F^α do not depend on z'. The actual variation in the value of P for different bulk materials is taken into account[26] by adjusting the parameter γ_c on the diagonal of the conduction band part of the Hamiltonian so that its eigenenergies yield a conduction band effective mass which is in agreement with the experimental value (see Appendix A). A similar correction should

also be applied for the zone center so band effective mass, but the effect of this is very small, especially for the upper valence subbands.

Once the Hamiltonian is known explicitly for the (001) growth direction it is straightforward to show that, by using $\mathbf{k}'=R\mathbf{k}$, for any other (hkl) growth direction the matrices $D^{\alpha\beta}$ and F^{α} in Eq. (4) are given by

$$D^{\alpha\beta}_{hkl}=\sum_{\alpha'\beta'} R_{\alpha\alpha'}D^{\alpha'\beta'}_{001}R^{-1}_{\beta'\beta}, \tag{6}$$

$$F^{\alpha}_{hkl}=\sum_{\alpha'} F^{\alpha'}_{001}R^{-1}_{\alpha'\alpha}. \tag{7}$$

We note that this transformation does not alter the set of basis function (1). In Sec. II B we will show that for the characterization of the hole states in QW structures grown along a direction other than (001) the basis (1) is not a convenient basis, but one should use a symmetry-adapted set of basis functions, i.e., basis functions which are adapted to the direction of growth.

When the energy gap between the conduction and the valence band is sufficiently large, the coupling between conduction and valence band states is small and can be taken into account perturbatively. This leads to the 6×6 Luttinger Kohn (LK) Hamiltonian[19] for valence band states, expanded in terms of the six valence band basis functions $u_3(\mathbf{r}')\cdots u_8(\mathbf{r}')$, to which we will refer as the LK basis in the following. The complete 8×8 Hamiltonian is of the form

$$H_K(z')=\begin{bmatrix} H_c(z') & C \\ C^{\dagger} & H_v(z') \end{bmatrix}, \tag{8}$$

where $H_c(z')$ and $H_v(z')$ are the 2×2 conduction band part and the 6×6 valence band part of $H_K(z')$, respectively, and C is a 2×6 rectangular matrix which represents the second (linear) term on the right hand side of Eq. (4) and describes the coupling between conduction and valence band states. Then, using perturbation theory, the LK Hamiltonian is found to be

$$H_{\mathrm{LK}}(z')=H_v(z')+\frac{C^{\dagger}C}{E_g(z')}. \tag{9}$$

We note that $H_{\mathrm{LK}}(z')$ does not contain anymore terms which linearly depend on the wave vector components, so that, in its general form in the style of (4) the second term vanishes. As shown in Appendix A, Eq. (9) amounts to a renormalization of the Luttinger parameters.

Finally, if one is only interested in the upper valence subbands and the splitoff gap Δ_{so} is large relative to the confinement energy of these states, then one may neglect the influence of the splitoff band and solve the 4×4 Luttinger Kohn Hamiltonian $H_{\Gamma_8}(z')$ which is obtained from $H_{\mathrm{LK}}(z')$ simply by deleting the last two rows and columns. The solutions are then expansions in terms of the Γ_8 basis $u_3(\mathbf{r}')\cdots u_6(\mathbf{r}')$. Note that a perturbative inclusion of the split-off band would lead to terms of order four in the wave vector components.

B. Characterization of the hole states and optical transition strength

For layered structures grown in the (001) direction, the 4×4 LK Hamiltonian is diagonal at $\mathbf{k}_{\parallel}=0$ and one can identify pure heavy hole (hh) and light hole (lh) states. By adding the conduction and/or the splitoff bands, the hh states remain pure but the lh states mix with the conduction and/or the so states at $\mathbf{k}_{\parallel}=0$. The mixing with the conduction states decreases for increasing E_g and is small for all cases considered in this paper. For lh states with a confinement energy which is small relative to Δ_{so}, also the mixing with the so states is small, so that these states retain a strongly dominant lh character. One may expect this to be true also in presence of strain since the strain Hamiltonian relative to the hh and lh basis functions is diagonal (see Sec. II C). However, the strain Hamiltonian gives an additional, relatively strong, coupling between lh and so states, so that, for strongly strained materials, even the highest lh states may be considerably mixed with so states at the zone center.

For growth directions other than (001), the characterization of the hole states is more complicated, since, in general, even the 4×4 LK Hamiltonian without strain, is not diagonal anymore at $\mathbf{k}'_{\parallel}=0$, independent of the choice of the basis (1). This means that, in general, one cannot find a transformation which diagonalizes the Hamiltonian for each layer. This holds *a fortiori* if the strain is included, as it will be shown in Sec. II C. Therefore, we need to answer the question whether one can identify hh and lh states at $\mathbf{k}'_{\parallel}=0$ also for growth directions other than (001). This is also important to generalize the selection rules for optical transitions as we will see at the end of this section.

Now, we show how, by a concomitant transformation of the Hamiltonian and of the basis functions (1), one can arrive for all growth directions to a natural definition of hh, lh, and so states which have exactly the same selection rules for light incoming parallel or perpendicular to the interfaces as in the (001) case. The only difference will be that, with the exception of the (001) and (111) directions, the hh and lh states will not be exactly decoupled at $\mathbf{k}'_{\parallel}=0$. This fact will be shown to have interesting effects on the optical properties, the most striking being a dependence of the matrix elements for optical transitions on the in-plane light polarization.

To this purpose, we find it convenient to go back to the $\mathbf{k}\cdot\mathbf{p}$ Hamiltonian relative to the basis $|X\rangle$, $|Y\rangle$, and $|Z\rangle$, $D_{XYZ}(\mathbf{k})$, which does not take into account the spin-orbit coupling:[27]

TABLE I. GaAs perpendicular hh effective masses $m^*_{\perp\mathrm{hh}}$ [Eq. (16)] for three families of (hkl) growth directions.

(hkl)	$m^*_{\perp\mathrm{hh}}$	(hkl)	$m^*_{\perp\mathrm{hh}}$	(hkl)	$m^*_{\perp\mathrm{hh}}$
(111)	0.952	(011)	0.690	(111)	0.952
(112)	0.690	(012)	0.531	(122)	0.814
(113)	0.527	(013)	0.451	(133)	0.750
(114)	0.463	(014)	0.419	(144)	0.724
(115)	0.432	(015)	0.404	(155)	0.712
...		...		...	
(001)	0.377	(001)	0.377	(011)	0.690

$$D_{XYZ}(\mathbf{k})=-\begin{bmatrix} Lk_x^2+M(k_y^2+k_z^2) & Nk_xk_y & Nk_xk_z \\ Nk_yk_x & Lk_y^2+M(k_x^2+k_z^2) & Nk_yk_z \\ Nk_zk_x & Nk_zk_y & Lk_z^2+M(k_x^2+k_y^2) \end{bmatrix}, \tag{10}$$

where L, M, and N have the following relations with the Luttinger parameters:

$$L=\frac{\hbar^2}{2m_0}(\gamma_1+4\gamma_2),$$

$$M=\frac{\hbar^2}{2m_0}(\gamma_1-2\gamma_2),$$

$$N=\frac{\hbar^2}{2m_0}6\gamma_3. \tag{11}$$

The 6×6 LK Hamiltonian is obtained from D_{XYZ} by calculating the matrix elements relative to the LK basis $[u_3(\mathbf{r})\cdots u_8(\mathbf{r})]$, adding E_v to all diagonal positions and including the spin-orbit coupling by adding $-\Delta_{\rm so}$ to the last two diagonal positions. Note that the spin-orbit coupling is diagonal relative to the LK basis. The matrix D_{XYZ} can be separated in three terms as follows:

$$D_{XYZ}(\mathbf{k})=-\frac{\hbar^2}{2m_0}\Big[(\gamma_1-2\gamma_2)k^2I_3+6\gamma_3\mathbf{k}\mathbf{k}^T +6(\gamma_2-\gamma_3)\sum_{\alpha=x,y,z}\hat{\mathbf{e}}_\alpha\hat{\mathbf{e}}_\alpha^T k_\alpha^2\Big], \tag{12}$$

where I_3 is the 3×3 unit matrix and $\hat{\mathbf{e}}_x$, $\hat{\mathbf{e}}_y$, and $\hat{\mathbf{e}}_z$ are the orthonormal column unit vectors (1,0,0), (0,1,0), and (0,0,1), respectively. If we transform the wave vector according to $\mathbf{k}'=R\mathbf{k}$ and at the same time apply an orthogonal basis transformation of the basis functions $|X\rangle$, $|Y\rangle$, and $|Z\rangle$ to the rotated basis functions $|X'\rangle$, $|Y'\rangle$, and $|Z'\rangle$ according to the same transformation R [Eq. (5)] such that $|Z'\rangle$ is oriented in the direction (hkl), then $D_{XYZ}(\mathbf{k})$ transforms as

$$D_{XYZ}(\mathbf{k})\rightarrow RD_{XYZ}(R^{-1}\mathbf{k}')R^{-1}\equiv D'_{X'Y'Z'}(\mathbf{k}'). \tag{13}$$

It is easy to show that the first two terms on the right hand side of the expression (12) are invariant by this transformation. In fact, omitting the constants, the first term transforms to $k'^2RI_3R^{-1}=k'^2I_3$, and the second term transforms to $RR^{-1}\mathbf{k}'(R^{-1}\mathbf{k}')^TR^{-1}=\mathbf{k}'\mathbf{k}'^T$ (using $R^{-1}=R^T$). The third term is, in general, not invariant and transforms as

$$\sum_{\alpha=x,y,z}\hat{\mathbf{e}}_\alpha\hat{\mathbf{e}}_\alpha^T k_\alpha^2\rightarrow\sum_{\alpha,\beta,\gamma=x,y,z}R\hat{\mathbf{e}}_\alpha(R\hat{\mathbf{e}}_\alpha)^TR_{\beta\alpha}R_{\gamma\alpha}k'_\beta k'_\gamma$$

$$\equiv\sum_{\alpha=x,y,z}\hat{\mathbf{e}}_\alpha\hat{\mathbf{e}}_\alpha^T k'^2_\alpha+\Delta D_{hkl}(\mathbf{k}'), \tag{14}$$

where $\Delta D_{hkl}(\mathbf{k}')$ represents the difference with the expression before the transformation. Corresponding to the transformation R, we define the transformed basis functions $u'_3(\mathbf{r}')\cdots u'_8(\mathbf{r}')$ as in (1) but with $|X\rangle$, $|Y\rangle$, $|Z\rangle$ replaced by $|X'\rangle$, $|Y'\rangle$, $|Z'\rangle$ and where the spin-quantization axis coincides with the (hkl) direction. Relative to these transformed basis functions, which we will call the symmetry-adapted LK basis in the following [the basis (1) is symmetry-adapted only for the (001) growth direction], the LK Hamiltonian can be written as

$$H'_{\rm LK}=H_{\rm LK}+\Delta H_{hkl}, \tag{15}$$

where the correction term ΔH_{hkl} is due to the term $-(\hbar^2/2m_0)6(\gamma_2-\gamma_3)\Delta D_{hkl}$. We note that also in the symmetry-adapted LK basis the spin-orbit coupling is diagonal. Since ΔH_{hkl} is proportional to $\gamma_2-\gamma_3$, it vanishes in the axial approximation (i.e., $\gamma_2=\gamma_3$). This means that, in the axial approximation, the in-plane band structure for a layered structure does not depend on the growth direction, so that we have to abandon the axial approximation to search for changes depending on the growth direction. Interesting changes can be expected, in particular when the well-acting material has a large difference between γ_2 and γ_3, i.e., has a strongly warped bulk band structure. Explicit expressions for the rotated Hamiltonian in the restricted four-dimensional hh and lh basis for the specific case of (h11) growth are given in Ref. 6.

At this point, it makes sense to generalize the meaning of hh, lh, and so states for a layered structure grown in an arbitrary direction (hkl), defining them with respect to the symmetry-adapted basis. We define $u'_3(\mathbf{r}')$ and $u'_4(\mathbf{r}')$ as basis functions for hh states, $u'_5(\mathbf{r}')$ and $u'_6(\mathbf{r}')$ for lh states and the remaining two for so states. This is a natural definition, since it yields exactly the same selection rules for optical transitions with respect to incoming light parallel and perpendicular to the layers as for the (001) growth direction. Moreover, the eigenstates at $\mathbf{k}'_\parallel=0$ can be expected to be close to pure hh and lh states for any growth direction according to this definition, since ΔH_{hkl} is in general small relative to $H_{\rm LK}$ so that the mixing of hh and lh states at the zone center is small.

Once the definition of hh and lh states is generalized, we first derive analytical expressions for effective masses and then assess how the mixing of hh and lh states at $\mathbf{k}'_\parallel=0$ depends on the growth direction. By use of the symmetry-adapted basis, the effective masses for hh and lh bands in the limit of uncoupled bands can be found from the diagonal terms of H'_{LK}. The effective masses in perpendicular direction [i.e., (hkl) direction], governing size quantization, are given by

$$m^*_{\perp\rm hh}=[\gamma_1-2\gamma_2+3(\gamma_2-\gamma_3)d_{\rm hh}]^{-1}, \tag{16}$$

$$m^*_{\perp lh}=[\gamma_1+2\gamma_2+(\gamma_2-\gamma_3)d_{\rm lh}]^{-1}, \tag{17}$$

where

$$d_{\rm hh}=2c_1^2c_3^2(h^4+k^4+h^2k^2)l^2+2c_2^2c_3^2h^2k^2, \quad (18)$$

$$d_{\rm lh}=d_{\rm hh}+4c_3^4(h^4+k^4+l^4)-4. \quad (19)$$

Extremal values occur for the (001) direction, where $m^*_{\perp\rm hh}=(\gamma_1-2\gamma_2)^{-1}$ and $m^*_{\perp\rm lh}=(\gamma_1+2\gamma_2)^{-1}$ and for the (111) direction, where $m^*_{\perp\rm hh}=(\gamma_1-2\gamma_3)^{-1}$ and $m^*_{\perp\rm lh}=(\gamma_1+2\gamma_3)^{-1}$. If we restrict ourselves to the yz plane, extremal values occur for the (001) and the (011) directions, where in the latter case we have $m^*_{\perp\rm hh}=(\gamma_1-\gamma_2/2-3\gamma_3/2)^{-1}$ and $m^*_{\perp\rm lh}=(\gamma_1+\gamma_2/2+3\gamma_3/2)^{-1}$. In the planes, spanned by any two of the (001), (111), and (011) high symmetry directions, the effective masses behave monotonously when going from one to the other high symmetry direction, as shown in Table I for the heavy hole effective masses of GaAs.

The in-plane effective masses [perpendicular to the (hkl) direction] in the uncoupled band limit along the generic in-plane direction $\hat{\mathbf{n}}=(n_1,n_2,0)$ (where $n_1^2+n_2^2=1$) are

$$m^*_{\parallel\rm hh}(\mathbf{n})=[n_1^2\gamma_{\rm hh}^{xx}+2n_1n_2\gamma_{\rm hh}^{xy}+n_2^2\gamma_{\rm hh}^{yy}]^{-1}, \quad (20)$$

$$m^*_{\parallel\rm lh}(\mathbf{n})=[n_1^2\gamma_{\rm lh}^{xx}+2n_1n_2\gamma_{\rm lh}^{xy}+n_2^2\gamma_{\rm lh}^{yy}]^{-1}, \quad (21)$$

where

$$\begin{aligned}\gamma_{\rm hh}^{xx}&=\gamma_1+\gamma_2+3(\gamma_2-\gamma_3)d_{\rm hh}^{xx},\\ \gamma_{\rm hh}^{xy}&=3(\gamma_2-\gamma_3)d_{hh}^{xy},\\ \gamma_{\rm hh}^{yy}&=\gamma_1+\gamma_2+3(\gamma_2-\gamma_3)d_{\rm hh}^{yy},\end{aligned} \quad (22)$$

$$\begin{aligned}\gamma_{\rm lh}^{xx}&=\gamma_1-\gamma_2+(\gamma_2-\gamma_3)d_{\rm lh}^{xx},\\ \gamma_{\rm lh}^{xy}&=(\gamma_2-\gamma_3)d_{\rm lh}^{xy},\\ \gamma_{\rm lh}^{yy}&=\gamma_1-\gamma_2+(\gamma_2-\gamma_3)d_{\rm lh}^{yy},\end{aligned} \quad (23)$$

and

$$\begin{aligned}d_{\rm hh}^{xx}&=c_1^4(l^4h^4+l^4k^4+(h^2+k^2)^4)+2c_1^2c_2^2h^2k^2l^2-1,\\ d_{\rm hh}^{xy}&=c_1^3c_2(hk^3-h^3k)l^3+c_1c_2^3(h^3k-hk^3)l,\\ d_{\rm hh}^{yy}&=c_2^4(h^4+k^4)+2c_1^2c_2^2h^2k^2l^2-1,\\ d_{\rm lh}^{xx}&=d_{\rm hh}^{xx}+8c_1^2c_3^2(h^4+k^4+h^2k^2)l^2,\\ d_{\rm lh}^{xy}&=d_{\rm hh}^{xy}-4c_1c_2c_3^2(h^2-k^2)hkl,\\ d_{\rm lh}^{yy}&=d_{\rm hh}^{yy}+8c_2^2c_3^2h^2k^2.\end{aligned} \quad (24)$$

$$\quad (25)$$

For $(hkl)=(001)$, where R [Eq. (5)] is not well-defined, we have to take $d_{\rm hh}^{\alpha\beta}=d_{\rm lh}^{\alpha\beta}=0$ $(\alpha,\beta=x,y,z)$. The terms of the form $k'_\parallel(d/dz')$ also contribute to the in-plane effective mass, as we show in Appendix C, but in first order perturbation for a symmetric QW this contribution vanishes due to the parity of the envelope function at $\mathbf{k}'_\parallel=0$.

It is possible to obtain $\Delta D_{hkl}(\mathbf{k}')$ explicitly in terms of h, k, l, and of the wave vector components. For the purpose of ascertaining for which growth directions the hh and lh states are decoupled at $\mathbf{k}'_\parallel=0$, here we give it explicitly for $\mathbf{k}'_\parallel=0$:

$$\Delta D_{hkl}=k_z'^2\begin{bmatrix}d_{11}&d_{12}&d_{13}\\ d_{21}&d_{22}&d_{23}\\ d_{31}&d_{32}&d_{33}\end{bmatrix}, \quad (26)$$

where

$$\begin{aligned}d_{11}&=2c_1^2c_3^2(h^4+k^4+h^2k^2)l^2,\\ d_{22}&=2c_2^2c_3^2h^2k^2,\\ d_{33}&=c_3^4(h^4+k^4+l^4)-1,\\ d_{12}&=d_{21}=-c_1c_2c_3^2(h^2-k^2)hkl,\\ d_{13}&=d_{31}=c_1c_3^3(h^4l+k^4l-h^2l^3-k^2l^3),\\ d_{23}&=d_{32}=-c_2c_3^3(h^2-k^2)hk.\end{aligned} \quad (27)$$

The $\mathbf{k}\cdot\mathbf{p}$ Hamiltonian relative to the symmetry-adapted Γ_8 basis $u'_3(\mathbf{r}')\cdots u'_6(\mathbf{r}')$ has pure hh and lh eigenstates at the zone center whenever $d_{12}=d_{13}=d_{23}=0$ and $d_{11}=d_{22}$, since in that case we have at $\mathbf{k}'_\parallel=0$ that $\langle X'+iY'|\hat{H}_{\mathbf{k}\cdot\mathbf{p}}|X'-iY'\rangle=\langle X'+iY'|\hat{H}_{\mathbf{k}\cdot\mathbf{p}}|Z'\rangle=0$ so that the 4×4 LK Hamiltonian is diagonal. Apart from the (001) direction (where $\Delta D_{001}=0$) this is only the case for the (111) direction, where $d_{11}=d_{22}=1/3$, $d_{33}=-2/3$, and $d_{12}=d_{13}=d_{23}=0$. For all growth directions other than (001) and (111) there is a small residual coupling (proportional to $\gamma_2-\gamma_3$) between hh and lh states. However, neglecting these relatively small off-diagonal terms at $\mathbf{k}'_\parallel=0$ provides a way to label the hh and lh states in an unique way according to their confinement energy for any growth direction. The small residual couplings between the hh and lh states, of the form d^2/dz'^2, do not couple hh and lh states with opposite parity in a symmetrical QW structure; since the coupling between two states depends on their separation in energy, the strongest coupling can be expected for the $\rm hh_1$ and the $\rm lh_1$ state. However, in general, even in this case, the states still have a dominant hh or lh character (as we will demonstrate in Sec. III).

For $(hkl)=(111)$, the coupling of the hh and lh states with the so and/or conduction band states at $\mathbf{k}'_\parallel=0$ is analogous to the (001) case. For (hkl) different from (001) or (111) instead, both hh and lh states are coupled with the so states. Although hh states do not couple directly with the conduction band, they do couple indirectly via the lh states and so states.

For the high symmetry directions (001) and (111) the strain Hamiltonian relative to the symmetry-adapted Γ_8 basis is diagonal (see Sec. II C) and does not lead to mixing of the hh and lh states. For other directions, the strain induces further mixing between hh, lh, and so states.

We are now able to assess selection rules for dipolar optical transitions for all growth directions in a unified way. The probability for interband optical transitions from a valence band state $\psi_v(\mathbf{r}')$ to a conduction band state $\psi_c(\mathbf{r}')$ is

proportional to the squared absolute value of $p_{vc}\equiv\hat{\boldsymbol{\epsilon}}'\cdot\mathbf{p}'_{vc}$, where $\hat{\boldsymbol{\epsilon}}'$ is the polarization vector of the light and

$$\mathbf{p}'_{vc}=\langle\psi_v|\mathbf{p}'|\psi_c\rangle \tag{28}$$

is the dipolar matrix element between the two states. The components of both $\hat{\boldsymbol{\epsilon}}'$ and $\mathbf{p}'_{vc}$ are expressed with respect to the rotated basis. Taking both states as solutions of the 8×8 Hamiltonian in the symmetry-adapted basis and considering light incoming perpendicular to the layers (i.e., $\epsilon_z=0$) we can write:[28]

$$\mathbf{p}'_{vc}\simeq\sum_{i,j=1}^{8}\langle u'_i|\mathbf{p}'|u'_j\rangle\int_{-\infty}^{\infty}\phi'^{*}_{vi}(z')\phi'_{cj}(z')dz', \tag{29}$$

where $\langle u'_i|\mathbf{p}'|u'_j\rangle=1/\Omega_0\int_{\Omega_0}u'^{*}_i(\mathbf{r}')\mathbf{p}'u'_j(\mathbf{r}')d\mathbf{r}'$ (with Ω_0 the volume of the bulk unit cell) and $\phi'_1(z')\cdots\phi'_8(z')$ are the envelope function components occurring in the expansion in terms of symmetry-adapted basis functions. If we label the conduction, hh and lh bound states at $\mathbf{k}'_\parallel=0$ by the integers n_c, $n_{\rm hh}$, and $n_{\rm lh}$ according to their confinement energies, then, for a symmetric potential $V(z')$, we have that $n_c-n_{\rm hh}$ and $n_c-n_{\rm lh}$ should be even to have nonvanishing transition probabilities at $\mathbf{k}'_\parallel=0$, as a consequence of the parity of the envelope functions. It is easy to show that the eigenstates at $\mathbf{k}'_\parallel=0$ have the property that either the conduction band envelope functions are even and the valence band envelope functions odd or vice versa. The strongest transitions are those with $n_c-n_{\rm hh}=0$ and those with $n_c-n_{\rm lh}=0$. The above selection rules apply for any growth direction.

Furthermore, for (001)-oriented heterostructures, it is well-known that the transition probability is independent of the in-plane polarization of the light, since $|\langle\psi_v|p_x|\psi_c\rangle|^2=|\langle\psi_v|p_y|\psi_c\rangle|^2$, and that the hh-$c$ transitions are about three times stronger than the lh-c transitions, since $|\langle u_c|p_{x/y}|u_{\rm hh}\rangle|^2=3|\langle u_c|p_{x/y}|u_{\rm lh}\rangle|^2$. Conversely, for growth directions other than (001) and (111), due to the mixing between hh and lh states, the transition probabilities will not be anymore independent of the linear polarization of the light in the plane, and the probability for the ${\rm hh}_n$-c_n transition may be different from three times the probability for the corresponding ${\rm lh}_n$-c_n transition. This anisotropic behavior is demonstrated in Sec. III for the ${\rm hh}_1$-c_1 and ${\rm lh}_1$-c_1 transitions for various QW's.

C. Strain and piezoelectricity

The deformation introduced by the lattice mismatch between the constituent materials in a heterostructure is characterized by the deformation tensor S, defined through

$$\hat{\mathbf{v}}'_\alpha=\sum_{\beta=x,y,z}(\delta_{\alpha\beta}+S_{\alpha\beta})\hat{\mathbf{v}}_\beta, \tag{30}$$

where $\hat{\mathbf{v}}_x$, $\hat{\mathbf{v}}_y$, and $\hat{\mathbf{v}}_z$ are orthonormal vectors along the edges of the simple cubic cell. For a generic growth direction, S contains a symmetric and an antisymmetric part:[24]

$$S=\boldsymbol{\epsilon}+A, \tag{31}$$

where the symmetric part $\boldsymbol{\epsilon}$ is the strain tensor and the antisymmetric part A, which vanishes for the high symmetry (001), (011), and (111) growth directions, describes a rigid rotation of the deformed crystal. We note that the presence of a nonvanishing antisymmetric part of S indicates that there is shear strain since an asymmetric (real) matrix cannot be diagonalized by a real orthogonal basis transformation. The matrix elements of S are fixed by minimization of the mean elastic energy density with the constraint(s) that the in-plane lattice parameters match at the interface(s). The mean elastic energy density for a heterostructure made of l layers is given by

$$\bar{U}=\frac{1}{L}\sum_l d_l U_l, \tag{32}$$

where d_l is the width of layer l, $L=\Sigma_l d_l$, and U_l is the elastic energy density in layer l given by

$$\begin{aligned}U_l=&\frac{1}{2}C_{11}(\epsilon^2_{lxx}+\epsilon^2_{lyy}+\epsilon^2_{lzz})+C_{12}(\epsilon_{lxx}\epsilon_{lyy}+\epsilon_{lxx}\epsilon_{lzz}\\&+\epsilon_{lyy}\epsilon_{lzz})+2C_{44}(\epsilon^2_{lxy}+\epsilon^2_{lxz}+\epsilon^2_{lyz}),\end{aligned} \tag{33}$$

where $\epsilon_{l\alpha\beta}=1/2(S_{l\alpha\beta}+S_{l\beta\alpha})$ and C_{11}, C_{12}, and C_{44} are elastic constants. Note that the antisymmetric part of S does not contribute to the energy density. It only contributes in the sense that it may (and for low symmetry growth directions it does) lead to a lower minimal value for the elastic energy. Writing the zinc-blende primitive basis vectors for the layer l as

$$\begin{aligned}\mathbf{b}_{l1}&=\frac{a_l}{2}(\hat{\mathbf{v}}_x+\hat{\mathbf{v}}_y),\\\mathbf{b}_{l2}&=\frac{a_l}{2}(\hat{\mathbf{v}}_x+\hat{\mathbf{v}}_z),\\\mathbf{b}_{l3}&=\frac{a_l}{2}(\hat{\mathbf{v}}_y+\hat{\mathbf{v}}_z),\end{aligned} \tag{34}$$

where a_l is the bulk lattice parameter for the layer l, the primitive lattice basis vectors of the deformed material are given by $\mathbf{b}'_{li}=(I+S_l)\mathbf{b}_{li}$ (i=1,2,3) and the six constraints due to the matching at the interface between the layers l and $l+1$ can be written as

$$\begin{aligned}\mathbf{b}'_{li}\cdot\hat{\mathbf{n}}_1&=\mathbf{b}'_{l+1i}\cdot\hat{\mathbf{n}}_1,\\\mathbf{b}'_{li}\cdot\hat{\mathbf{n}}_2&=\mathbf{b}'_{l+1i}\cdot\hat{\mathbf{n}}_2\end{aligned} \tag{35}$$

for $i=1,2,3$ where $\hat{\mathbf{n}}_1$ and $\hat{\mathbf{n}}_2$ are two orthonormal vectors in the plane of the layers, for example given by the first two rows of the rotation matrix R [Eq. (5)] for growth directions other than (001). The boundary conditions have to be applied for all interfaces. Since the width of the substrate on which a layered structure is grown is usually very much larger than the layers of interest, the deformation in the substrate will be negligible so that, if no relaxation takes place, the in-plane lattice parameters of each layer will match to that of the substrate and the minimization of $\bar{U}$ can be performed for each layer separately, giving the deformation tensors layer per layer.

For the high-symmetry (001), (011), and (111) growth directions, the deformation tensor is symmetric, and thus equal to the strain tensor, and can be shown to have the form

$$\begin{bmatrix} \epsilon_{xx} & 0 & 0 \\ 0 & \epsilon_{xx} & 0 \\ 0 & 0 & \epsilon_{zz} \end{bmatrix},$$

$$\begin{bmatrix} \epsilon_{xx} & 0 & 0 \\ 0 & \epsilon_{yy} & \epsilon_{yz} \\ 0 & \epsilon_{yz} & \epsilon_{yy} \end{bmatrix},$$

and

$$\begin{bmatrix} \epsilon_{xx} & \epsilon_{xy} & \epsilon_{xy} \\ \epsilon_{xy} & \epsilon_{xx} & \epsilon_{xy} \\ \epsilon_{xy} & \epsilon_{xy} & \epsilon_{xx} \end{bmatrix}, \tag{36}$$

respectively. This simplifies the constrained minimization of U by reducing the number of independent variables.

Once the strain tensor is known, the strain Hamiltonian H^{str} can be determined following Bir and Pikus.[30] Due to the strain, the momentum operator $\mathbf{p}=-i\hbar\boldsymbol{\nabla}$ transforms to $\mathbf{p}'=(I+S)^{-1}\mathbf{p}$. This affects the coupling matrix elements $\langle S|\mathbf{p}'_\alpha|X\rangle$ $\langle S|\mathbf{p}'_\alpha|Y\rangle$ and $\langle S|\mathbf{p}'_\alpha|Z\rangle$ $(\alpha=x,y,z)$ between the conduction and the valence band states and leads to slightly modified conduction and valence band effective masses.[29] However, the dependence of the coupling between conduction and valence band states on strain is quite small in general and therefore we shall neglect it in the following.

We choose to keep the energy of the conduction band edge fixed and let the valence band edge vary with strain. Note that the relative positions of the various band edges for different layers in a QW structure is determined by the valence band offset(s).

From symmetry considerations[30] it follows that the strain Hamiltonian relative to the $L=1$ basis functions $|X\rangle$, $|Y\rangle$, and $|Z\rangle$, H^{str}_{XYZ}, has the following form:

$$H^{\mathrm{str}}_{XYZ}=\begin{bmatrix} l_s\epsilon_{xx}+m_s(\epsilon_{yy}+\epsilon_{zz}) & n_s\epsilon_{xy} & n_s\epsilon_{xz} \\ n_s\epsilon_{yx} & l_s\epsilon_{yy}+m_s(\epsilon_{xx}+\epsilon_{zz}) & n_s\epsilon_{yz} \\ n_s\epsilon_{zx} & n_s\epsilon_{zy} & l_s\epsilon_{zz}+m_s(\epsilon_{xx}+\epsilon_{yy}) \end{bmatrix}, \tag{37}$$

where l_s, m_s, and n_s are related to the hydrostatic deformation potential a and to the uniaxial deformation potentials b and d by

$$l_s=-a+2b,$$

$$m_s=-a-b,$$

$$n_s=\sqrt{3}d. \tag{38}$$

In Appendix B the strain Hamiltonian relative to the LK basis $[u_3(\mathbf{r})\cdots u_8(\mathbf{r})]$ given in Eq. (1), $H^{\mathrm{str}}_{\mathrm{LK}}$ is given explicitly. This Hamiltonian has to be added to the valence band part of the $\mathbf{k}\cdot\mathbf{p}$ Hamiltonian.

For the (001) growth direction the strain Hamiltonian relative to the Γ_8 basis is diagonal. There is a constant energy shift $-a(2\epsilon_{xx}+\epsilon_{zz})$ of the whole valence band (hydrostatic term) plus an additional shift $\pm b(\epsilon_{xx}-\epsilon_{zz})$ for the hh and the lh band edge, respectively, breaking the degeneracy. Furthermore, there is a relatively strong strain-induced coupling between lh and so states.

For (hkl) $\neq$ (001) the basis set (1) is not the symmetry-adapted basis; for non-(001)-oriented structures the strain Hamiltonian relative to the symmetry-adapted basis can be found by first calculating it relative to the rotated basis functions $|X'\rangle$, $|Y'\rangle$, and $|Z'\rangle$ according to

$$H^{\mathrm{str}}_{X'Y'Z'}=RH^{\mathrm{str}}_{XYZ}R^{-1}. \tag{39}$$

It is easy to show that the strain Hamiltonian relative to the symmetry-adapted Γ_8 basis for the hh and lh states is diagonal whenever $H^{\mathrm{str}}_{X'Y'Z'}$ is diagonal and the elements on the first two diagonal positions (of $H^{\mathrm{str}}_{X'Y'Z'}$) are equal. In general, this is only the case for the (111) growth direction [apart from the (001) direction], where we find [using (36)]:

$$H^{\mathrm{str}}_{X'Y'Z'}=\begin{bmatrix} -3a\epsilon_{xx}-\sqrt{3}d\epsilon_{xy} & 0 & 0 \\ 0 & -3a\epsilon_{xx}-\sqrt{3}d\epsilon_{xy} & 0 \\ 0 & 0 & -3a\epsilon_{xx}+2\sqrt{3}d\epsilon_{xy} \end{bmatrix}. \tag{40}$$

This form is similar to that for the (001) direction and yields a constant energy shift $-3a\epsilon_{xx}$ for the valence band plus an additional shift $\mp\sqrt{3}d\epsilon_{xy}$ for the hh and lh band edges, respectively. As for the (001) direction, there is relatively strong coupling between lh and so states.

For growth directions other than (001) and (111), the dominant terms of the strain Hamiltonian in the symmetry-adapted LK basis are the strain-induced shifts of the valence band edges, breaking the degeneracy of the hh and lh band edge in the same way as for the (001) and (111) direction, and the relatively strong coupling between the lh and so states, but in addition there are residual couplings between

hh and lh states and between hh and so states. However, in general, these residual couplings are considerably weaker than the lh-so coupling.

The presence of nonzero off-diagonal strain tensor components gives rise to an internal electric polarization, since the zinc-blende structure allows the piezoelectric effect; for symmetry reasons this effect appears only for growth directions other than (001). Using the conventions indicated, e.g., by Nye,[31] we evaluate the components of the strain-induced piezoelectric polarization $\mathbf{P}^s$ relative to the simple cubic frame as given by

$$P^s_\alpha = e_{\alpha\beta\gamma}\epsilon_{\beta\gamma} \tag{41}$$

for $\alpha = x,y$, and z where $e_{\alpha\beta\gamma}$ are the piezoelectric constants, $\epsilon_{\beta\gamma}$ the components of the strain tensors, and we have used the summation convention on repeated indices. Making use of the fact that both $e_{\alpha\beta\gamma}$ and $\epsilon_{\beta\gamma}$ are symmetrical in β and γ, expression (41) can be rewritten in Voigt's notation as

$$P^s_\alpha = \sum_{n=1}^{6} e_{\alpha n}\epsilon_n , \tag{42}$$

where the indices $n = 1-6$ correspond to xx, yy, zz, yz, xz, and xy, respectively. For the zinc-blende crystal structure, the only nonzero piezoelectric constants are $e_{x4} = e_{y5} = e_{z6} = 2e_{xyz}$ and we have

$$P^s_x = e_{x4}\epsilon_4 ,$$

$$P^s_y = e_{x4}\epsilon_5 ,$$

$$P^s_z = e_{x4}\epsilon_6 , \tag{43}$$

From this the component of $\mathbf{P}^s$ perpendicular to the layers is easily obtained:

$$P^s_\perp = e_{x4}(h\epsilon_4 + k\epsilon_5 + l\epsilon_6)/c_3 . \tag{44}$$

The piezoelectric polarization introduces dipole charges at the interface planes, which cause a piezoelectric field $\mathbf{E}$. This field, in turn, introduces another contribution to the polarization, so that the total polarization $\mathbf{P}$ becomes

$$\mathbf{P} = \epsilon_0\chi\mathbf{E} + \mathbf{P}^s, \tag{45}$$

where χ is the susceptibility of the material. Furthermore, we have the electrodynamical relation:

$$\mathbf{D} = \epsilon_0\mathbf{E} + \mathbf{P} \tag{46}$$

which together with Eq. (45) leads to

$$\mathbf{D} = \epsilon_0\epsilon_r\mathbf{E} + \mathbf{P}^s, \tag{47}$$

where $\epsilon_r = (1+\chi)$ is the relative dielectric constant of the material. The vector field $\mathbf{D}$ obeys Maxwell's equation $\nabla\cdot\mathbf{D} = \rho_e$, which, assuming that there is no external charge (i.e., $\rho_e = 0$) leads to the boundary condition that $D_\perp$ is constant over the interface. Then from Eq. (47) we find the following relation for the electrostatic potential $\Phi(z')$:

$$\epsilon_0\left(\epsilon_r^{l+1}\frac{d\Phi_{l+1}}{dz'} - \epsilon_r^{l}\frac{d\Phi_l}{dz'}\right) = -(P^s_{\perp\,l+1} - P^s_{\perp\,l}), \tag{48}$$

where l labels the layers in the heterostructure. It follows that $\Phi(z')$ is a linear function of z' and that its derivative has discontinuities at the interfaces. Then $\Phi(z')$ is completely fixed by using the short circuit condition:

$$\int_0^L E_\perp(z')dz' = 0, \tag{49}$$

where L is the total length of the sample. For a single QW, assuming that the well layer is in the interval $[(L-W)/2,(L+W)/2]$ and that the width of the barriers is very much larger than that of the well, so that the field in the barriers is negligible, we obtain the following potential:

$$\Phi(z) = \begin{cases} -\dfrac{P^s_\perp}{\epsilon_0\epsilon_r}\dfrac{W}{2}, & z' \in [0,(L-W)/2), \\ \dfrac{P^s_\perp}{\epsilon_0\epsilon_r}\left(z' - \dfrac{L}{2}\right), & z' \in [(L-W)/2,(L+W)/2] , \\ \dfrac{P^s_\perp}{\epsilon_0\epsilon_r}\dfrac{W}{2}, & z' \in ((L+W)/2,L] \end{cases} \tag{50}$$

where $P^s_\perp$ and ϵ_r are relative to the well layer. This expression is in agreement with previously published results.[23,34]

It appears that the piezoelectric potential is strongest for the (111) growth direction. For instance, for a 60 Å $In_{0.25}Ga_{0.75}As/Al_{0.4}Ga_{0.6}As$ QW grown in the (111) direction, we evaluate a potential drop over the well of 99 meV, whereas for the same QW grown in the (113) direction the potential drop is only 28.5 meV. For the (011) growth direction $P_\perp = 0$ and $\Phi(z')$ vanishes.

The piezoelectric potential $\Phi(z')$ must be added on the diagonal of the Hamiltonian. For a structure which is inversion symmetric with respect to the z' coordinate, $\Phi(z')$ breaks the symmetry and, as a consequence of this, the spin degeneracy of the states for $\mathbf{k}'_\parallel \neq 0$.

The total Hamiltonian $H^{\rm tot}(z')$, containing the $\mathbf{k}\cdot\mathbf{p}$ part and both contributions from the strain, is given by

$$H^{\rm tot}(z') = H^{\mathbf{k}\cdot\mathbf{p}}(z') + H^{\rm str}(z' =) + \Phi(z')I_m, \tag{51}$$

where I_m is the identity matrix of order m, which is the number of band edge basis function involved.

D. Solution method

To find the in-plane band structure near the band gap for a QW structure, with or without strain, we have to solve a coupled second order differential eigenvalue equation. To this purpose, we propose a discretization method which is different from the straightforward finite difference method and which is known as the finite element method. Instead of using finite difference expressions for the first and second order derivatives of envelope functions at each point of a grid, the starting point of our method is to assume a linear behavior of the envelope functions on intervals. By fixing N points $z_1' \cdots z_N'$, not necessarily equidistant, within the total interval $[0,L]$ containing the QW structure, the envelope functions and their derivatives in the interval $z_n' < z' \leqslant z_{n+1}'$ are written as

$$\vec{\phi}(z') = \vec{\phi}_n + \frac{(z'-z_n')}{\Delta_n}(\vec{\phi}_{n+1} - \vec{\phi}_n), \tag{52}$$

$$\vec{\phi}'(z') = \frac{(\vec{\phi}_{n+1} - \vec{\phi}_n)}{\Delta_n}, \tag{53}$$

where the components of $\vec{\phi}_n = \vec{\phi}(z_n')$ represent the values of the envelope functions at the points z_n' and $\Delta_n = z_{n+1}' - z_n'$. For QW structures, the total interval $[0,L]$ is chosen such that for confined states $|\vec{\phi}(L/2 \pm L/2)|$ is sufficiently small, so that in practice we may put infinite potential barriers at $z' = L/2 \pm L/2$. Typically a value of $L = 5W$, with two barriers of width $2W$ at both sides of a well of width W, is sufficiently large for the structures considered in this paper.

We define the functionals $F[\vec{\phi}(z')]$ and $C[\vec{\phi}(z')]$ by

$$F[\vec{\phi}(z')] = \int_0^L \vec{\phi}^\dagger(z') H^{tot} \vec{\phi}(z'), \tag{54}$$

$$C[\vec{\phi}(z')] = \int_0^L \vec{\phi}^\dagger(z') \vec{\phi}(z'). \tag{55}$$

From constrained optimization, we deduce that the solutions of interest are those $\vec{\phi}(z')$ for which $F[\vec{\phi}(z')] - EC[\vec{\phi}(z')]$ has stationary values. The need of second order derivatives of the envelope functions in the evaluation of $F[\vec{\phi}(z')]$ can be avoided by partial integration using the fact that the envelope functions vanish far away from the well. Typically, $\mathbf{k}\cdot\mathbf{p}$ Hamiltonians contain operators of the form $(d/dz')\,\gamma\,(d/dz')$ and we can rewrite:

$$\int_0^L \phi_i^\dagger(z') \frac{d}{dz'} \left(\gamma \frac{d}{dz'} \phi_j(z') \right) = -\int_0^L \left(\frac{d}{dz'} \phi_i^\dagger(z') \right) \gamma \frac{d}{dz'} \phi_j(z'). \tag{56}$$

This relationship holds for superlattices as well, since, in that case, the boundary terms vanish due to the periodic boundary conditions. By use of (52), (53), and (56), the integrals (54) and (55) can be evaluated piecewise on the small intervals and F and C can be expressed in terms of the values of the envelope functions at the discrete points $\vec{\phi}_1 \cdots \vec{\phi}_N$:

$$F(\ldots,\vec{\phi}_n,\ldots) = \sum_{n,n'=1}^{N} \vec{\phi}_n^\dagger A_{nn'} \vec{\phi}_{n'}$$

$$C(\ldots,\vec{\phi}_n,\ldots) = \sum_{n,n'=1}^{N} \vec{\phi}_n^\dagger B_{nn'} \vec{\phi}_{n'}, \tag{57}$$

where A is a sparse Hermitian band matrix of the order mN with m the number of envelope functions and B a real band matrix of the form $T_n \otimes I_m$, where I_m is the identity matrix of the order m and T_N is a real symmetric tridiagonal matrix of order N. More explicitly, we find $B_{nn} = 1/3(\Delta_{n-1} + \Delta_n) I_m$ and $B_{nn'} = 1/6(\Delta_n) I_m$ for $n' = n \pm 1$.

In the case of a superlattice the band form of A and B is lost because of the edge terms. From constrained optimization we finally obtain the following generalized eigenvalue problem:

$$\sum_{n'=1}^{N} A_{nn'} \vec{\phi}_{n'} = E \sum_{n'=1}^{N} B_{nn'} \vec{\phi}_{n'}, \tag{58}$$

for which we have to find the energy eigenvalues E of interest, i.e., those lying in the energy range yielding confined states. These eigenvalues can be found quite efficiently either by using band matrix algorithms or by using the Lanczos algorithm.[33] The band routines cannot be used for superlattices.

The significative advantage of the finite element method over the finite difference method is that discontinuities of the potential and of the band parameters at the interface are taken into account ''exactly'' and that there is ''correct'' matching of the envelope functions at the interface. In the finite difference method, the discontinuities have to be approximated by sharp slopes requiring an increased density of grid points at the interface. To avoid very large matrices it is desirable to vary the distances between the grid points. In the finite difference method this leads to a non-Hermitian eigenvalue problem (58); analogously, non-Hermiticity results also from discontinuities of the effective masses in going from one layer to the other. In the finite elements method instead, since the calculation of the matrix elements $A_{nn'}$ and $B_{nn'}$ is done piecewise on small intervals which do not contain any discontinuities, the Hermiticity is maintained also when considering variable distances between the grid points and when there are variations of the band parameters across the interfaces. This is a useful property, because, on the one hand, it allows to enlarge the intervals in the barriers where the envelope functions decay rapidly, reducing the order of the eigenvalue problem (58) and, on the other hand, yields automatically physically significant solutions.

III. RESULTS: BAND STRUCTURE, EFFECTIVE MASSES, HOLE-MIXING, OPTICAL TRANSITION STRENGTHS

We present results concerning the electronic structure of single QW's for various growth directions, with and without

TABLE II. Bulk parameters used in this paper. The value of $E_p=(2/m_0)|P|^2$ (see Appendix A) is taken equal to 22.71 eV for each of the layer materials considered in this paper. All parameters are obtained from Ref. 35, except for the AlAs lattice parameter from Ref. 36.

	GaAs	AlAs	InAs	GaP
a (Å)	5.6534	5.6614	6.0570	5.4506
E_g (eV)	1.519	3.13	0.418	2.890
Δ_{so} (eV)	0.341	0.321	0.380	0.080
m_c^*	0.0665	0.0230	0.1240	0.1700
γ_1	6.85	3.45	19.67	4.05
γ_2	2.10	0.68	8.37	0.49
γ_3	2.90	1.29	9.29	1.25
C_{11} (10^{12} dyn/cm^2)	1.2110	1.2500	0.8329	1.4390
C_{12} (10^{12} dyn/cm^2)	0.5480	0.5340	0.4526	0.6520
C_{44} (10^{12} dyn/cm^2)	0.6040	0.5420	0.3959	0.7143
a (eV)	-7.00	-7.00	-6.00	-8.83
b (eV)	-1.70	-1.70	-1.80	-1.50
d (eV)	-4.55	-4.55	-3.60	-4.60
ϵ_r	12.91	10.06	15.15	10.88
l_{14} (10^{-4} C/cm^2)	-0.1600	-0.1600	-0.0459	-0.1000

strain. In all cases, we assume a GaAs substrate so that the in-plane lattice parameter of both well and barriers is always taken as that of GaAs. We consider unstrained GaAs/$Al_xGa_{1-x}As$, compressively strained $In_xGa_{1-x}As/Al_xGa_{1-x}As$ and tensilely strained $GaP_xAs_{1-x}/Al_yGa_{1-y}As$ QW's. In all cases the barriers are made of $Al_xGa_{1-x}As$ and are therefore only slightly strained.

All the relevant bulk structural and electronic constants used in this paper are given in Table II.[35,36] The value of P is taken equal for each layer material considered here and corresponds to a value of $E_p=(2/m_0)|P|^2$ equal to 22.71 eV. For ternary materials, these constants are obtained by linear interpolation, except for the energy gap which is assumed to vary as $E_g=E_{g1}x+E_{g2}(1-x)-Cx(1-x)$, with $C=0.370$ for the $Al_xGa_{1-x}As$, $C=0.475$ for the $In_xGa_{1-x}As$ and $C=0.170$ for the $GaAs_{1-x}P_x$ compounds and where E_{g1} and E_{g2} are the gaps of the pure materials. For the GaAs/$Al_xGa_{1-x}As$ QW's, we use a valence band offset $\Delta E_v/(\Delta E_g)=0.35$. For the other structures, the valence band offset is determined by the method of van de Walle.[37] We assume that the band offset is independent of the growth direction.[38] However, we note that, in presence of strain, the effective band offset for hh and lh states slightly varies as a function of the growth directions since the effect of strain depends on the growth direction.[39]

A. Unstrained quantum wells

In this section, we present the electronic structure as a function of the growth direction for a 120 Å GaAs/$Al_{0.3}Ga_{0.7}As$ QW, where the well remains unstrained. We have checked that the effect of the strain in the barriers is negligible.

Figure 1 displays the valence subband dispersion for six growth directions along the two in-plane directions $(1'0'0')$ and $(1'1'0')$. We remind that primed indices are relative to the rotated basis defined by the transformation R [Eq. (5)]. In all cases the subbands are obtained from the 6×6 LK Hamiltonian, but for the (001) and the (113) growth directions also the results obtained by using the 8×8 and the 4×4 model are shown for comparison. It can be seen that the influence of the splitoff band is noticeable only on the lower subbands and at large $\mathbf{k}_\parallel'$ and that inclusion of the conduction band has a very minute effect for this material. Furthermore, we observe that the confinement energies for hh states at $\mathbf{k}_\parallel'=0$ are largest for the (001) direction and smallest for the (111) direction. The opposite is true for lh states, resulting in the inversion of the lh_1 and hh_2 levels; the confinement energy of the lh_1 state is smaller than that of the hh_2 only for the (001) direction. This behavior

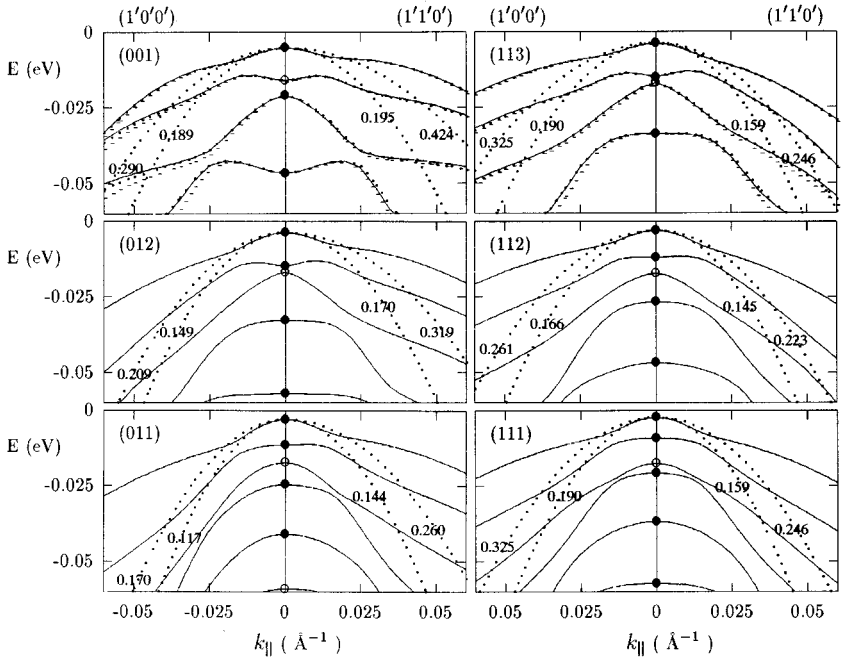

FIG. 1. Hole-dispersion along the $(1'0'0')$ and $(1'1'0')$ in-plane directions for a 120 Å GaAs/$Al_{0.3}Ga_{0.7}As$ QW grown along either the (001), (012), (011), (111), (112), and (113) directions calculated by use of the 6×6 LK Hamiltonian (solid lines). For the (001) and (113) growth directions, the results obtained by use of the 8×8 (dotted lines) and the 4×4 (dashed lines) **k·p** Hamiltonians also are shown. Closed and open dots at $k_\parallel'=0$ indicate hh and lh subbands, respectively. The parabolic dotted lines are best fits on the $k_\parallel'$ intervals $[0,\pi/2L]$ and $[0,\pi/L]$ and the values written on it represent the corresponding effective masses.

TABLE III. Perpendicular hh and lh effective masses [Eqs. (16) and (17)] for the well- and barrier-acting materials and the corresponding energy levels of the first four confined states at $\mathbf{k}_\parallel'=0$ of a 120 Å $GaAs/Al_{0.3}Ga_{0.7}As$ QW in the uncoupled band approximation. The values in brackets are the values obtained from the full LK Hamiltonian, including the off-diagonal coupling terms.

(hkl)	$m^{*w}_{\perp \mathrm{hh}}$	$m^{*b}_{\perp \mathrm{hh}}$	$m^{*w}_{\perp \mathrm{lh}}$	$m^{*b}_{\perp \mathrm{lh}}$	E_1	E_2	E_3	E_4
(001)	0.377	0.403	0.091	0.109	5.26	16.51	20.96	46.82
					(5.26)	(16.11)	(20.96)	(46.82)
(011)	0.690	0.731	0.082	0.097	3.09	12.33	17.87	27.69
					(2.91)	(11.37)	(17.26)	(24.51)
(111)	0.952	1.004	0.079	0.094	2.30	9.21	18.31	20.72
					(2.30)	(9.21)	(17.58)	(20.72)
(113)	0.527	0.561	0.085	0.101	3.92	15.66	17.37	35.09
					(3.80)	(15.14)	(16.98)	(33.85)

can be quite well explained in terms of the perpendicular effective masses obtained from Eqs. (16) and (17). In Table III, we give their numerical values for four growth directions both for the well- and the barrier-acting material. Extremal perpendicular effective masses occur for the (001) and the (111) direction. Since the confinement energies at $\mathbf{k}_\parallel'=0$ are roughly proportional to the inverses of the perpendicular masses, the results of Fig. 1 are qualitatively in agreement with the masses in Table III.

If we use the effective masses of Table III and we neglect the off-diagonal terms in the Hamiltonian we obtain uncoupled equations for hh and for lh levels. The hh_1, hh_2, hh_3, and lh_1 levels resulting at $\mathbf{k}_\parallel'=0$ within this approximation are also given in Table III and compared with the numerical values obtained from the full Hamiltonian (values in brackets). In all cases, the uncoupled band values for the first three confined states differ by less than 1 meV from the values obtained by solving the full Hamiltonian. This means that very good approximations of the first hh and lh energy levels at $\mathbf{k}_\parallel'=0$ can be easily obtained for any growth direction by solving the particle-in-a-box problem[21] with effective masses given by Eqs. (16) and (17).

Also, the in-plane effective masses depend considerably on the direction of confinement, as can be seen from the parabolic fits in Fig. 1. These parabolas are obtained from best fits on the intervals $[0,\pi/2L]$ and $[0,\pi/L]$, where $L=120$ Å is the QW width. The lightest averaged in-plane effective mass is observed for the (111) direction. Partially this is due to the fact that the second subband is also a hh subband resulting in a decreased anticrossing effect between the first two subbands.

A first order approximation for the effective mass for the hh subbands in the in-plane direction $\hat{\mathbf{n}}$ in the limit of uncoupled subbands is given by

$$m^*_{\parallel \mathrm{hh}}(\hat{\mathbf{n}})=\left[\frac{1-P_b}{m^{*w}_{\parallel \mathrm{hh}}(\hat{\mathbf{n}})}+\frac{P_b}{m^{*b}_{\parallel \mathrm{hh}}(\hat{\mathbf{n}})}\right]^{-1}, \tag{59}$$

where $m^{*w}_{\parallel \mathrm{hh}}(\hat{\mathbf{n}})$ and $m^{*b}_{\parallel \mathrm{hh}}(\hat{\mathbf{n}})$ are the values obtained from Eq. (20) for the well and the barrier, respectively, and P_b is the integrated probability over the barriers for the wave function at $\mathbf{k}_\parallel'=0$. The same expression can be written for lh subbands. If the valence band offset between well and barriers and the QW width are not too small then P_b is small for the hh_1 state, so that it is a good approximation to set it to zero in (59) yielding $m^*_{\parallel \mathrm{hh}}(\hat{\mathbf{n}})=m^{*w}_{\parallel \mathrm{hh}}(\hat{\mathbf{n}})$. For the QW considered here we find $P_b<0.03$ for each growth direction.

The in-plane effective masses for hh subbands as obtained from Eq. (20) for the well-acting material are given in Table IV for four growth directions. These values deviate considerably from the values obtained from the parabolic fits over the interval $[0,\pi/2L]$, given in Fig. 1, and even from the values obtained from a numerical fit at $\mathbf{k}_\parallel'\sim 0$ (values in parentheses in Table IV). This is obviously due to the coupling between the subbands, in particular, the coupling introduced by the matrix elements of the form $k_\parallel' d/dz'$ which strongly couple hh and lh states with opposite parity. In second order perturbation, this coupling gives a contribution proportional to $k_\parallel'^2$ to the energy, so that it forms a direct contribution to the effective mass at $\mathbf{k}_\parallel'\sim 0$ and also adds to the anisotropy. For a more precise approximation of the in-plane effective mass for the hh_1 subband at $\mathbf{k}_\parallel'\sim 0$, one should take into account the interaction of this subband with the lh_2 subband. Nevertheless the first order values listed in Table IV are useful guidelines, also for the anisotropy.

The warping can be further studied by equal energy contour plots. In Fig. 2 we show the equal energy contours of the hh_1 subband for the same growth directions as in Fig. 1. The

TABLE IV. Parallel hh effective masses [Eq. (20)] in the $(1'0'0')$, $(1'1'0')$, and $(0'1'0')$ in-plane directions for GaAs compared with the numerical values obtained from a fit at $\mathbf{k}_\parallel'\sim 0$ for a 120 Å $GaAs/Al_{0.3}Ga_{0.7}As$ QW (values in parentheses).

(hkl)	$m^*_{\parallel \mathrm{hh}}(1'0'0')$	$m^*_{\parallel \mathrm{hh}}(1'1'0')$	$m^*_{\parallel \mathrm{hh}}(0'1'0')$
(001)	0.112 (0.168)	0.112 (0.171)	0.112 (0.168)
(011)	0.099 (0.108)	0.105 (0.137)	0.112 (0.181)
(111)	0.103 (0.131)	0.103 (0.131)	0.103 (0.131)
(113)	0.105 (0.155)	0.107 (0.156)	0.109 (0.162)

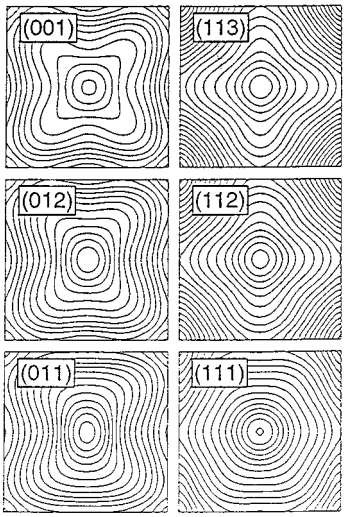

FIG. 2. Equal energy contour plots for the hh_1 subband obtained by use of the 6×6 LK Hamiltonian for the same structure and growth directions as in Fig. 1. The energy spacing of the contours is 1 meV.

(111) direction displays the most isotropic behavior, the strongest warping occurring for the (011) and (012) directions. For the latter two, the warping is already present at $\mathbf{k}_\parallel' \sim 0$, in agreement with the uncoupled band values given in Table IV.

Each of the pictures in Fig. 2 shows mirror symmetry, due to the fact that, in real space, for each of the growth directions there is a mirror symmetry with respect to a plane perpendicular to the plane of the layers. In addition, the (001) direction displays fourfold and the (111) direction sixfold symmetry, in agreement with the symmetry in real space. The (112) and (113) directions both tend to fourfold symmetry, as the (001) direction. The warping is somewhat stronger for the (113) than for the (112) direction, the latter being ''closer'' to the isotropic (111) direction.

We have also calculated the character of the eigenstates in the generalized sense as a function of $\mathbf{k}_\parallel'$. In Fig. 3 the squared absolute values of the projections of the eigenstates on the hh, lh, and so symmetry-adapted basis functions summed over the two spin states are shown for the first three confined states for the (001), (011), (111), and (113) growth directions. Apart from some quantitative variations, the results are quite similar for each growth direction. At $\mathbf{k}_\parallel' = 0$ the eigenstates have either a pure or a dominant hh or lh character. Away from $\mathbf{k}_\parallel' = 0$, the states start to have a strongly mixed character. Since the subbands cannot cross, this mixing can be partially explained in terms of anticrossing effects. A more careful study of the character of the states at $\mathbf{k}_\parallel' = 0$ reveals that for the (001) and the (111) directions these states are pure hh and lh states apart from the mixing of the lh states with the so states, which is very small for the first confined lh state. For the (011) and the (113) directions, instead, there is mixing between hh and lh states also at $\mathbf{k}_\parallel' = 0$, in agreement with the theory in Sec. II B.

It appears that this mixing gives rise to a considerable dependence of the optical transition matrix element p_{vc} on the linear in-plane polarization of the light coming in perpendicular to the layers. This anisotropy is shown for the (011) and the (113) growth directions in Fig. 4 where $|p_{vc}|^2$ is plotted as a function of $\mathbf{k}_\parallel'$ for the two helicities of circular polarization as well as for linearly polarized light along the in-plane x' and y' directions. The result for the (001) direction, which is similar to that of the (111) direction, is shown for comparison. The range of $\mathbf{k}_\parallel'$ vectors in Fig. 4 is comparable to $1/a_b$, where a_b is the excitonic Bohr radius in GaAs. Here we have not explicitly determined the exciton wave function, but since this wave function is, roughly speaking, made up of states belonging to $\mathbf{k}_\parallel'$ vectors within the range $1/a_b$ we can conclude from Fig. 4 that the in-plane anisotropy should not be removed by excitonic effects at least for the (011) growth direction. Experimental evidence of this behavior has been very recently reported in Ref. 40 for (011)-grown structures.

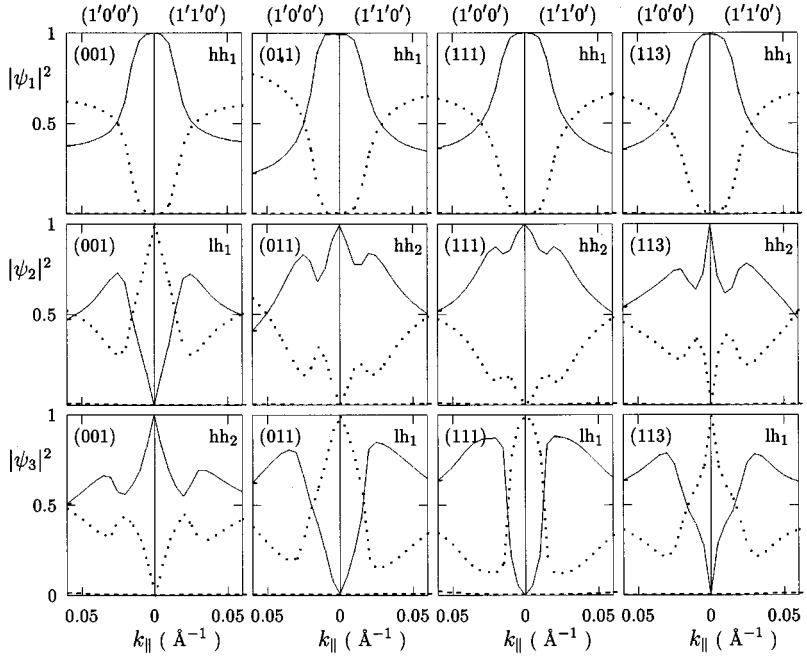

FIG. 3. The hh (solid lines), lh (dotted lines), and so (dashed lines) contributions to the integrated squared wave function for the first three confined states as a function of $\mathbf{k}_\parallel'$ in the same in-plane directions and for the same structure as in Fig. 1 for the (001), (011), (111), and (113) growth directions. Notice that the lh_1 subband is the third subband for all growth directions but the (001).

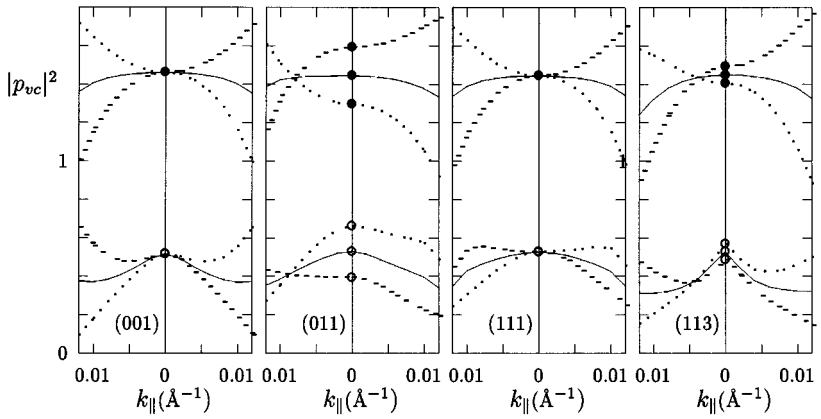

FIG. 4. Squared absolute value of the optical transition matrix element p_{vc} for the two circular light polarizations (solid line) and for linearly polarized light (dashed and dotted lines for polarization in the x' and y' directions, respectively), incoming perpendicular to the layers, for the hh_1-c_1 (closed dots) and lh_1-c_1 transitions (open dots) as a function of $\mathbf{k}_\parallel'$ in the $(1'0'0')$ (left hand side) and $(0'1'0')$ (right hand side) in-plane directions and for the same structures as in Fig. 1 and the same growth directions as in Fig 3.

Obviously, the anisotropy shown in Fig. 4 is due to an in-plane anisotropy of the wave function. To check this point, we expand the eigenstates in the following way:

$$|\psi\rangle=\sum_{\alpha\sigma} F_{\alpha\sigma}(z')|\alpha\sigma\rangle, \tag{60}$$

where $\alpha=S,X',Y',Z'$ are the rotated spatial basis functions and $\sigma=\uparrow,\downarrow$ indicates the spin state. Furthermore, we define the probability functions $P_\alpha(z')$ as

$$P_\alpha(z')=\sum_{\sigma} |F_{\alpha\sigma}(z')|^2 \tag{61}$$

for $\alpha=S,X',Y',Z'$. Differences in the $P_{X'}(z')$ and $P_{Y'}(z')$ components indicate anisotropy of the wave function in the plane. For the (001) and (111) growth direction, $P_{X'}(z')=P_{Y'}(z')$ at $\mathbf{k}_\parallel'=0$. In Fig. 5, the $P_\alpha(z')$ components are shown for the first hh and lh confined states at $\mathbf{k}_\parallel'=0$ for the (011) and (113) growth directions. The differences in the X' and Y' components are largest for the (011) case, in agreement with the stronger anisotropy of the transition matrix element in this case.

B. Compressively strained quantum well

A thin $\mathrm{In}_x\mathrm{Ga}_{1-x}\mathrm{As}$ layer grown on a GaAs substrate is compressively strained. In Fig. 6 we show the strain-induced energy shifts of the hh, lh, and so band edges as a function of the indium content x for various growth directions, where the conduction band edge is taken fixed. Hence, the total energy gap between the valence band edge and the conduction band edge is given by the hh shift indicated in Fig. 6 plus the energy gap for the unstrained material (also depending on x). Again, the (001) and the (111) growth directions show extremal behavior. At equal lattice mismatch the shifts are minimal for the (001) and maximal for the (111) growth direction. By adding these shifts to the diagonal of the Hamiltonian one can, neglecting all off-diagonal elements of the Hamiltonian, easily obtain good approximations for the energy levels of the first hh and lh confined states at $\mathbf{k}_\parallel'=0$ by solving the particle-in-a-box model[21] with the masses obtained from Eqs. (16) and (17) as we have shown in the previous section. For the lh states, however, this approximation is less reliable, because it neglects the strain-induced coupling between lh and so states.

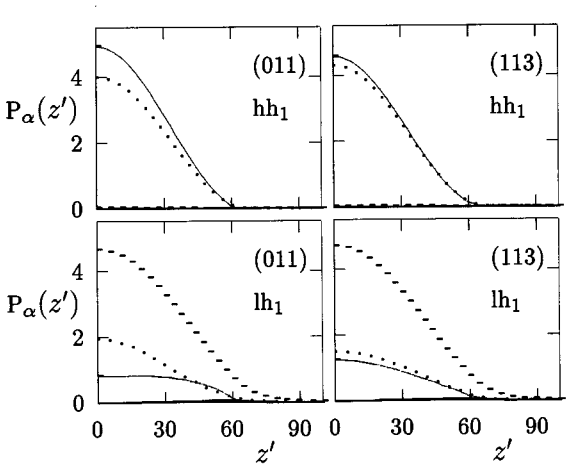

FIG. 5. Probability functions $P_{X'}(z')$ (solid lines), $P_{Y'}(z')$ (dotted lines), and $P_{Z'}(z')$ (dashed lines) (see text) for the first hh and lh confined states at $\mathbf{k}_\parallel'=0$ for the same structure as in Fig. 1 for the (011) and (113) growth directions. The center of the QW is taken as the origin of the z' coordinate.

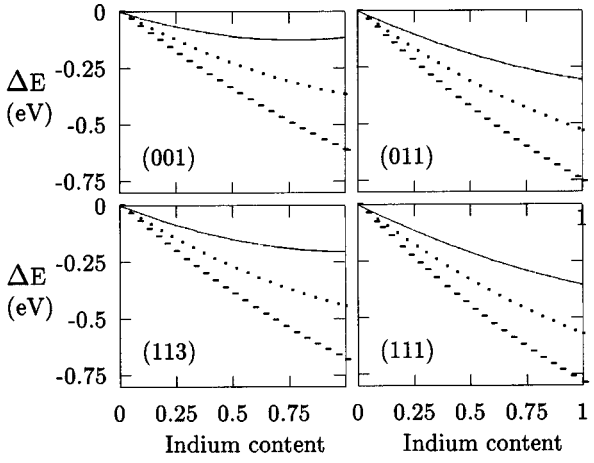

FIG. 6. Strain-induced energy shifts of hh (solid lines), lh (dashed lines), and so (dotted lines) band edges assuming a fixed conduction band edge for a compressively strained $\mathrm{In}_x\mathrm{Ga}_{(1-x)}\mathrm{As}$ layer grown on a GaAs substrate along the (001), (011), (111), and (113) directions.

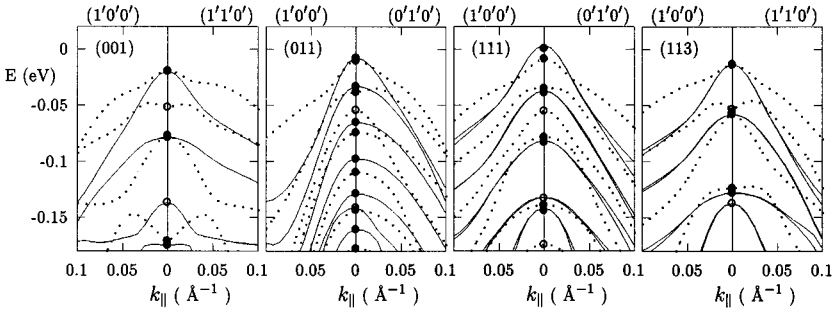

FIG. 7. Comparison between the in-plane hole-dispersion of a 60 Å compressively strained $In_{0.25}Ga_{0.75}As/Al_{0.4}Ga_{0.6}As$ QW (solid lines) and that of a 60 Å unstrained $GaAs/Al_{0.58}Ga_{0.42}As$ QW (dotted lines) grown along the (001), (011), (111), and (113) direction. Closed and open dots at $k_\parallel = 0$ indicate hh and lh subbands, respectively. The in-plane directions are indicated on the upper x axis.

Figure 7 shows, for several growth directions, the in-plane band structure of a 60 Å compressively strained $In_{0.25}Ga_{0.75}As/Al_{0.4}Ga_{0.6}As$ QW together with that of an unstrained $GaAs/Al_{0.58}Ga_{0.42}As$ QW of the same width. In all cases the zero of the energy is chosen as the hh band edge level in the middle of the QW (note that the hh band edge is not constant in the well in presence of a piezoelectric potential). The Al content for the unstrained QW is chosen such that both QW's have an almost equal band offset for the hh band edge for all growth directions. This, together with the fact that the perpendicular effective masses obtained from Eqs. (16) and (17) happen to be quite close for both well-acting materials, is the reason why the hh energy levels are so close for strained and unstrained QW's except for the (111) direction due the strong piezoelectric field occurring for the strained QW. For the (111) and (113) direction the strain causes a piezoelectric field which corresponds to a linear potential drop over the well of 99 and 28.5 meV, respectively. Apparently the piezoelectric potential causes a significant shift only of those energy levels which fall in the energy range over which the potential drop takes place.

For all growth directions, the lh levels for the strained QW have moved downwards relative to those of the unstrained QW. This is due to the larger shift of the lh band edge but also to the lighter lh perpendicular effective mass of the $In_{0.25}Ga_{0.75}As$ material. As a consequence, the anticrossing between the first two subbands, both hh-like, is weaker and the in-plane effective masses lighter. However, despite the increased separation between the hh_1 subband and the lh subbands, the in-plane effective masses for the hh_1 subband at $\mathbf{k}'_\parallel \sim 0$ are still much heavier than the uncoupled band values, as shown in Table V, where the effective masses obtained from Eq. (20) for the $In_{0.25}Ga_{0.75}As$ material are compared with the numerical values obtained by best fits at $\mathbf{k}'_\parallel \sim 0$ (values in parentheses). The deviations are due to the still large mixing with lh states. This is shown in Fig. 8, where the character distribution of the hh_1 subband states close to $\mathbf{k}'_\parallel = 0$ is shown for both the strained and the unstrained QW's. The mixing remains substantial and can even be increased for the strained QW as in the case of (011) growth, due to the strain-induced couplings.

Furthermore, for the (113) and (111) cases, the piezoelectric field causes a spin splitting which is rather small at $\mathbf{k}'_\parallel \sim 0$ but increases for larger $\mathbf{k}'_\parallel$ vectors, due to the increased mixed character of the states. In fact, spin splitting can only occur when states of different character start to mix, since in our Hamiltonian there is no coupling between the $-m_j$ and the $+m_j$ states, because we have neglected the relatively small k' and k'^3 terms which occur due to the inversion asymmetry of the zinc-blende structure.

In Fig. 9 we show the optical transition strength $|p_{vc}|^2$ for the (001)-, (011)-, (111)-, and (113)-grown strained QW's. It appears that the anisotropy, already observed for unstrained QW's in Fig. 4, is enhanced by strain. Moreover, while for unstrained (001)-grown QW's the ratio of the strengths for hh and lh transitions at $\mathbf{k}'_\parallel = 0$ is roughly 3:1 (see Fig. 4), this is not at all the case for the strained QW. Both these effects are due to the strong strain-induced coupling with the so band. The decrease of $|p_{vc}|^2$ for the strained (111)-grown QW is due to the built-in piezoelectric field, which makes that electronic states and hole states tend to localize at opposite sides of the well. For the same reason we find the c_1-hh_2 transition (not shown in Fig. 9), forbidden for a symmetric QW, to be about half as strong as the c_1-lh_1 transition. These transitions have also been observed experimentally.[41,42] For the (113) direction both of these effects are much weaker, due to the weaker piezoelectric field.

C. Tensilely strained quantum well

A situation of tensile strain occurs when, e.g., a GaP_xAs_{1-x} layer is grown on a GaAs substrate. In Fig. 10 we show the hh, lh, and so band edge energy shifts relative to the unstrained bulk levels, for fixed conduction band edge, as

TABLE V. Parallel hh effective masses [Eq. (20)] in the (1′0′0′), (1′1′0′), and (0′1′0′) in-plane directions for $In_{0.25}Ga_{0.75}As$ compared with the numerical values obtained from a fit at $\mathbf{k}'_\parallel \sim 0$ for a 60 Å $In_{0.25}Ga_{0.75}As/Al_{0.4}Ga_{0.6}As$ QW (values in parentheses).

(**hkl**)	$m^*_{\parallel hh}(1'0'0')$	$m^*_{\parallel hh}(1'1'0')$	$m^*_{\parallel hh}(0'1'0')$
(001)	0.073 (0.111)	0.073 (0.111)	0.073 (0.111)
(011)	0.070 (0.076)	0.071 (0.095)	0.072 (0.127)
(111)	0.069 (0.104)	0.069 (0.104)	0.069 (0.104)
(113)	0.067 (0.094)	0.070 (0.103)	0.073 (0.115)

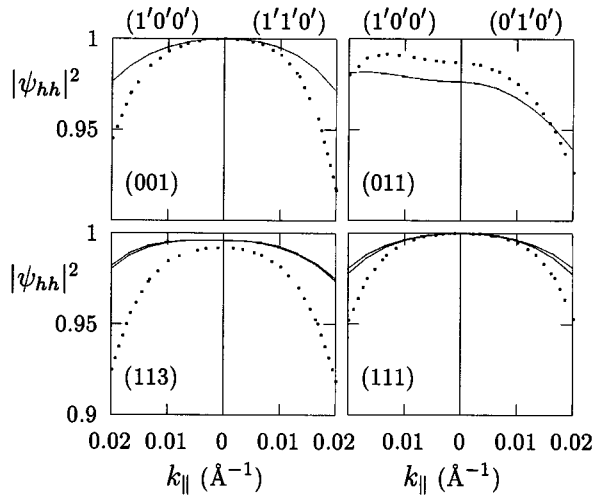

FIG. 8. The hh contribution to the integrated squared wave function as a function of small $\mathbf{k}'_\parallel$ vectors for the hh_1 subband for the same strained (solid lines) and unstrained (dotted lines) structures, the same in-plane directions and the same growth directions as in Fig. 7. Notice that, for the (011) growth direction, the strain has the effect of increasing the mixing with lh states.

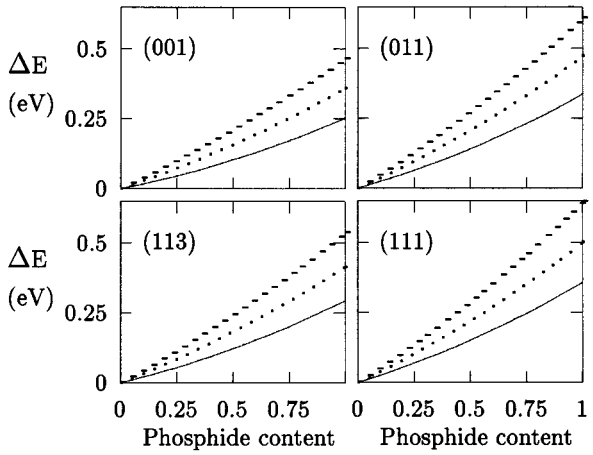

FIG. 10. Strain-induced energy shifts of hh (solid lines), lh (dashed lines), and so (dotted lines) band edges assuming a fixed conduction band edge for a tensilely strained $GaP_xAs_{(1-x)}$ layers grown on a GaAs substrate along the (001), (011), (111), and (113) directions.

a function of the phosphide content x for various growth directions. In contrast to the case of compressive strain, the highest band edge is the lh band edge. For the $GaP_xAs_{1-x}/Al_{0.4}Ga_{0.6}As$ QW's which we consider in this section, this means that for sufficiently strong strain (i.e., for large enough values of x) the first confined state will have a lh character.

This is shown in Fig. 11, where the in-plane band structure is shown for the (111) growth direction for $x=0.1$ and $x=0.2$. Whereas for $x=0.1$ the hh_1 state is still slightly above the lh_1 state, the situation is reversed for $x=0.2$. This inversion takes place for any growth directions, although at slightly different values of x.

For the structure of Fig. 11 the potential drop over the well due to the piezoelectric field is 33 meV for $x=0.1$ and 65 meV for $x=0.2$. This causes strong spin splittings where the subbands anticross, in agreement with the fact, already mentioned, that spin splitting can only occur for states with a mixed character at $\mathbf{k}'_\parallel \neq 0$. For $x=0.2$ the first two spin-split lh subbands are well above the next subbands whence their relatively small spin splitting as compared to the $x=0.1$ case.

For growth directions other than (001) and (111) the residual hh-lh coupling in the Hamiltonian at $\mathbf{k}'_\parallel = 0$ may lead to a strong mixing between the hh_1 and lh_1 states for a certain range of x values, when these two levels are close in energy. To check this effect, we show in Fig. 12 the calculated optical transition strength $|p_{vc}|^2$ at $\mathbf{k}'_\parallel = 0$ for perpendicular incoming circularly and linearly polarized light for transitions from the first two confined hole states to the first confined electronic state as a function of the phosphide content x in the interval [0.05,0.15] for the (011) growth direction. In spite of the hh-lh coupling, there is a rather abrupt inversion of the character of the states between $x=0.100$ and $x=0.105$. At both these values of x the energy separation between the first two confined states is less than 1 meV. However, whereas for $x=0.1025$ the first confined state has 99% hh character, for $x=0.105$ it has 94% lh character. An enhanced anisotropy is observed close to the inversion point. However, experimentally it would be hard to detect the anisotropy when the two levels are too close in energy.

Finally, Fig. 13 shows the optical transition strength as a function of $\mathbf{k}'_\parallel$ for $x=0.08$ and $x=0.12$ for the (011) growth direction. For $x=0.08$ the first confined state has a hh char-

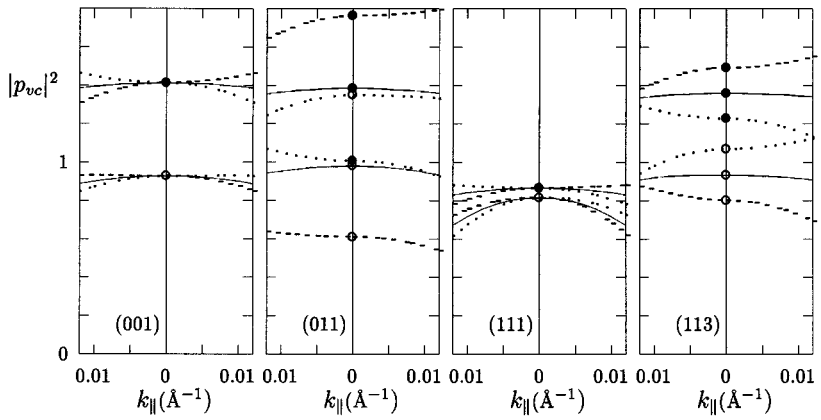

FIG. 9. Same as in Fig. 4 for a 60 Å compressively strained $In_{0.25}Ga_{0.75}As/Al_{0.4}Ga_{0.6}As$ QW. It can be seen that compressive strain enhances the anisotropic absorption for the (011) and (113) directions and changes the ratio between the hh_1-c_1 and the lh_1-c_1 transitions in all cases.

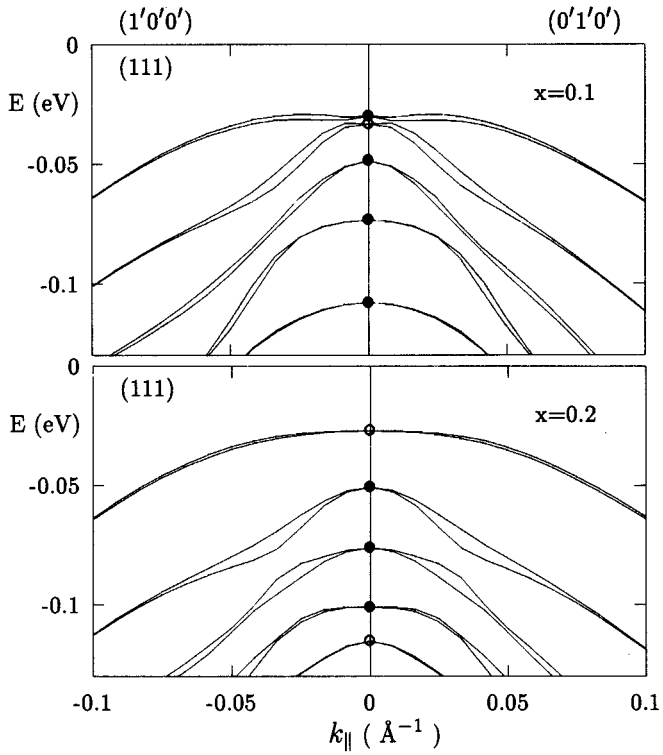

FIG. 11. Hole-dispersion along the $(1'0'0')$ and $(0'1'0')$ in-plane directions for a 80 Å tensilely strained $GaP_xAs_{1-x}/Al_{0.4}Ga_{0.6}As$ QW grown along the (111) direction for $x=0.1$ and $x=0.2$. Closed and open dots indicate hh and lh subbands at $\mathbf{k}'_\parallel=0$, respectively.

acter and lies 6.5 meV above the second confined state of lh character. Conversely, for $x=0.12$, the lh_1 state lies 5.5 meV above the hh_1 state. The behavior of $|p_{vc}|^2$ for $x=0.08$ results from the strong anticrossing between the first two subbands; whereas at $\mathbf{k}'_\parallel=0$ the first subband has hh character, it becomes lh-like immediately away from $\mathbf{k}'_\parallel=0$. This is due to the strong coupling (linear in $k'_\parallel$) between the lh_1 and the hh_2 states, yielding a positive in-plane effective mass of the

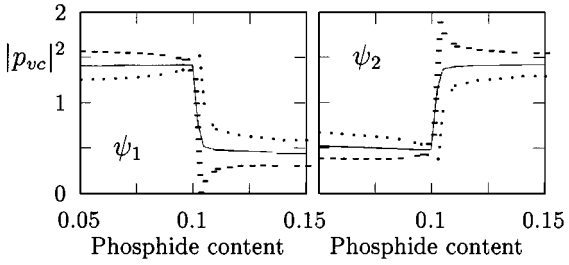

FIG. 12. Squared absolute value of the optical transition matrix-element p_{vc} at $\mathbf{k}'_\parallel=0$ for the transitions of the first two confined hole states (ψ_1 and ψ_2) to the first confined electronic state in a 80 Å $GaP_xAs_{1-x=}/Al_{0.4}Ga_{0.6}As$ QW grown in the (011) direction as a function of the phosphide content x for circularly (solid line) and linearly polarized light (dashed and dotted lines for polarization in the x' and y' directions, respectively), incoming perpendicular to the layers.

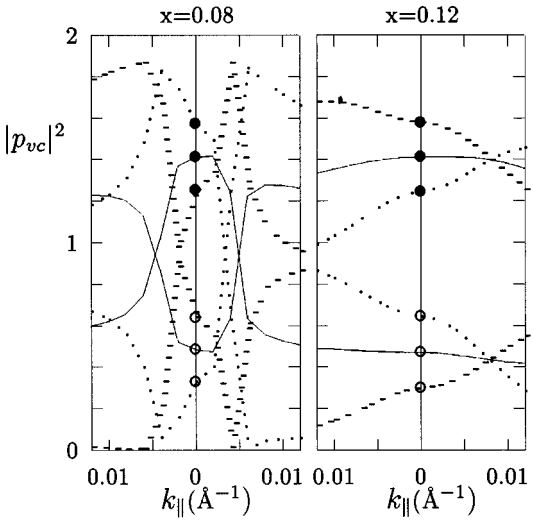

FIG. 13. Same as in Fig. 4 for a 80 Å tensilely strained $GaP_xAs_{1-=x}/Al_{0.4}Ga_{0.6}As$ QW grown in the (011) direction for $x=0.08$ and $x=0.12$.

lh_1 subband which causes the strong anticrossing with the hh_1 subband. For $x=0.12$ the lh_1 subband has become the highest in energy and the anticrossing with the hh_1 subband is strongly reduced.

IV. SUMMARY AND CONCLUSIONS

We have presented a comprehensive theoretical treatment of the electronic properties of strained and unstrained semiconductor QW structures grown along any (hkl) crystallographic directions. The numerical results, obtained by a very efficient, real-space, approach to the solution of the multiband Hamiltonian, point out the interest of growth on novel index planes for valence band engineering. Large differences in hole effective masses, warping and spin splittings are found to be induced by the crystallographic directions as well as by strain and piezoelectric fields.

We have also shown that, for any growth direction, one can identify dominant hh, lh, and so states at $\mathbf{k}'_\parallel=0$ by choosing a symmetry-adapted set of basis functions which yield exactly the same selection rules for optical transitions as those used for the usual (001) growth direction.

In the symmetry-adapted basis the **k·p** part of the total Hamiltonian can be separated in a part which is independent of the growth direction and a ''relatively small'' correction which varies with the growth direction, and which is responsible for a coupling of the hh states with the lh and so states at $\mathbf{k}'_\parallel=0$ for growth directions other than (001) and (111). An interesting consequence of this fact is the anisotropic behavior of the optical absorption as a function of the linear in-plane light polarization for perpendicular incoming light in the latter case. This anisotropy is enhanced by strain due to the strain-induced coupling with the so states.

Besides, we have derived analytical expressions for the effective masses in perpendicular and in-plane directions as a function of the (hkl) growth direction in the limit of uncoupled bands. Comparison to the exact numerical results shows the usefulness of these analytical expressions, particu-

larly in what concerns the quantization energy.

ACKNOWLEDGMENTS

This work has been carried out within the European Community HC&M network for High Pressure Studies of Semiconductors and Semiconductor Structures ERBCHRXCT 930321.

APPENDIX A

The 8×8 $\mathbf{k}\cdot\mathbf{p}$ Hamiltonian H_K relative to the basis functions (1) in Sec. II A and where k_x, k_y, and k_z are the coordinates in the (100), (010), and (001) directions, respectively, is given by

$$\begin{bmatrix}
E_c+\gamma_c k^2 & 0 & \sqrt{\frac{1}{2}}P'k_+ & 0 & -i\sqrt{\frac{2}{3}}P'k_z & \sqrt{\frac{1}{6}}P'k_- & \sqrt{\frac{1}{3}}P'k_z & -i\sqrt{\frac{1}{3}}P'k_- \\
0 & E_c+\gamma_c k^2 & 0 & \sqrt{\frac{1}{2}}P'k_- & \sqrt{\frac{1}{6}}P'k_+ & -i\sqrt{\frac{2}{3}}P'k_z & -i\sqrt{\frac{1}{3}}P'k_+ & \sqrt{\frac{1}{4}}P'k_z \\
\sqrt{\frac{1}{2}}P'k_- & 0 & E_v+p+q & 0 & l & m & i\sqrt{\frac{1}{2}}l & -i\sqrt{2}m \\
0 & \sqrt{\frac{1}{2}}P'k_+ & 0 & E_v+p+q & m^\dagger & -l^\dagger & -i\sqrt{2}m^\dagger & -i\sqrt{\frac{1}{2}}l^\dagger \\
i\sqrt{\frac{2}{3}}P'k_z & \sqrt{\frac{2}{3}}P'k_- & l^\dagger & m & E_v+p-q & 0 & -i\sqrt{2}q & i\sqrt{\frac{3}{2}}l \\
\sqrt{\frac{1}{6}}P'k_+ & i\sqrt{\frac{2}{3}}P'k_z & m^\dagger & -l & 0 & E_v+p-q & -i\sqrt{\frac{2}{3}}l^\dagger & -i\sqrt{2}q \\
\sqrt{\frac{1}{3}}P'k_z & i\sqrt{\frac{1}{3}}P'k_- & -i\sqrt{\frac{1}{2}}l^\dagger & i\sqrt{2}m & i\sqrt{2}q & i\sqrt{\frac{2}{3}}l & E_{\mathrm{so}}+p & 0 \\
i\sqrt{\frac{1}{3}}P'k_+ & \sqrt{\frac{1}{3}}P'k_z & i\sqrt{2}m^\dagger & i\sqrt{\frac{1}{2}}l & -i\sqrt{\frac{3}{2}}l^\dagger & i\sqrt{2}q & 0 & E_{\mathrm{so}}+p
\end{bmatrix} \tag{A1}$$

where

$$k_\pm = k_x \pm ik_y,$$

$$\gamma_c = \frac{\hbar^2}{2m_0}\left[\frac{m_0}{m_c^*} - \frac{2E_p}{3E_g} - \frac{E_p}{3(E_g+\Delta_{\mathrm{so}})}\right],$$

$$P' = \frac{\hbar}{m_0}P,$$

$$P = \langle S|p_x|X\rangle = \langle S|p_y|Y\rangle = \langle S|p_z|Z\rangle,$$

$$p = -\tilde{\gamma}_1\frac{\hbar^2}{2m_0}(k_x^2+k_y^2+k_z^2),$$

$$q = -\tilde{\gamma}_2\frac{\hbar^2}{2m_0}(k_x^2+k_y^2-2k_z^2),$$

$$l = i2\sqrt{3}\tilde{\gamma}_3\frac{\hbar^2}{2m_0}(k_x-ik_y)k_z,$$

$$m = \sqrt{3}\frac{\hbar^2}{2m_0}(\tilde{\gamma}_2 k_+ k_- - i2\tilde{\gamma}_3 k_x k_y). \tag{A2}$$

The parameters $\tilde{\gamma}_1$, $\tilde{\gamma}_2$, and $\tilde{\gamma}_3$ are the modified Luttinger parameters which are related to the Luttinger parameters by

$$\tilde{\gamma}_1 = \gamma_1 - \frac{E_p}{3E_g},$$

$$\tilde{\gamma}_2 = \gamma_2 - \frac{E_p}{6E_g},$$

$$\tilde{\gamma}_3 = \gamma_3 - \frac{E_p}{6E_g}, \tag{A3}$$

where $E_p = (2/m_0)|P|^2$.

The 6×6 LK Hamiltonian H_{LK} for valence band states is obtained from 6×6 valence band part of H_K by replacing the modified Luttinger parameters in the expressions (A2) by the Luttinger parameters.

To ensure the hermiticity of the Hamiltonian we have used the ''symmetrized'' form,[43] which means that we applied the following substitutions:

$$\gamma\frac{d^2}{dz^2} \rightarrow \frac{d}{dz}\gamma\frac{d}{dz}, \tag{A4}$$

$$-i\gamma\frac{d}{dz} \rightarrow -\frac{i}{2}\left\{\gamma, \frac{d}{dz}\right\} = -\frac{i}{2}\left(\gamma\frac{d}{dz} + \frac{d}{dz}\gamma\right). \tag{A5}$$

These substitutions lead to well-defined boundary conditions of the envelope functions at the interface(s). Recently, alternative boundary conditions, obtained from an exact derivation of the envelope function theory, have been presented.[44] In Refs. 45 and 46, it was shown that these modified bound-

ary conditions can lead to small differences in the subbands. Therefore we intend to adopt the exact form in the near future. We note, however, that the results presented in this paper do not change qualitatively by using the exact theory and that the theoretical analysis of the **k·p** Hamiltonian for different growth directions can easily be adapted to deal with the exact boundary conditions. The expressions for the effective masses Eqs. (16), (17), (20), and (21) remain unaffected.

APPENDIX B

The strain Hamiltonian relative to the six dimensional valence band part of basis (1) is given by

$$H_{\mathrm{LK}}^{\mathrm{str}}=\begin{bmatrix} \frac{r_1}{2} & 0 & \frac{-iw_2^*}{\sqrt{3}} & \frac{w_1^*}{\sqrt{12}} & \frac{w_2^*}{\sqrt{6}} & \frac{-iw_1^*}{\sqrt{6}} \\ 0 & \frac{r_1}{2} & \frac{w_1}{\sqrt{12}} & \frac{-iw_2}{\sqrt{3}} & \frac{-iw_1}{\sqrt{6}} & \frac{w_2}{\sqrt{6}} \\ \frac{iw_2}{\sqrt{3}} & \frac{w_1^*}{\sqrt{12}} & \frac{(r_1+4r_2)}{6} & 0 & \frac{-i(r_1-2r_2)}{\sqrt{18}} & \frac{w_2^*}{\sqrt{2}} \\ \frac{w_1}{\sqrt{12}} & \frac{iw_2^*}{\sqrt{3}} & 0 & \frac{(r_1+4r_2)}{6} & \frac{w_2}{\sqrt{2}} & \frac{-i(r_1-2r_2)}{\sqrt{18}} \\ \frac{w_2}{\sqrt{6}} & \frac{iw_1^*}{\sqrt{6}} & \frac{i(r_1-2r_2)}{\sqrt{18}} & \frac{w_2^*}{\sqrt{2}} & \frac{(r_1+r_2)}{3} & 0 \\ \frac{iw_1}{\sqrt{6}} & \frac{w_2^*}{\sqrt{6}} & \frac{w_2}{\sqrt{2}} & \frac{i(r_1-2r_2)}{\sqrt{18}} & 0 & \frac{(r_1+r_2)}{3} \end{bmatrix}, \tag{B1}$$

where the constants r_1, r_2, w_1, and w_2 are given by

$$r_1=\langle X+iY|\hat{H}^{\mathrm{str}}|X+iY\rangle=-(2a-b)(\epsilon_{xx}+\epsilon_{yy})-(2a+2b)\epsilon_{zz},$$

$$r_2=\langle Z|\hat{H}^{\mathrm{str}}|Z\rangle=-(a+b)(\epsilon_{xx}+\epsilon_{yy})-(a-2b)\epsilon_{zz},$$

$$w_1=\langle X-iY|\hat{H}^{\mathrm{str}}|X+iY\rangle=3b(\epsilon_{xx}-\epsilon_{yy})+i2\sqrt{3}d\epsilon_{xy},$$

$$w_2=\langle Z|\hat{H}^{\mathrm{str}}|X+iY\rangle=\sqrt{3}d\epsilon_{xz}+i\sqrt{3}d\epsilon_{yz}. \tag{B2}$$

We note that for growth directions other than (001) this is not the strain Hamiltonian in the symmetry-adapted basis.

APPENDIX C

Here, we extend the calculation of the in-plane effective mass for hh subbands in the uncoupled band approximation for an infinite square well [Eq. (20)] to include also the terms linear in d/dz'. Generally the eigenstates satisfy

$$\frac{\hbar^2}{2m_0}\left[-\gamma_{\mathrm{hh}}^{zz}\frac{d^2}{dz'^2}-i(\gamma_{\mathrm{hh}}^{xz}k_x'+\gamma_{\mathrm{hh}}^{yz}k_y')\frac{d}{dz'}+(\gamma_{\mathrm{hh}}^{xx}k_x'^2+2\gamma_{\mathrm{hh}}^{xy}k_x'k_y'+\gamma_{\mathrm{hh}}^{xx}k_y'^2)+V(z')\right]\phi_{hh}(z')=E\phi_{\mathrm{hh}}(z'), \tag{C1}$$

where $\gamma_{\mathrm{hh}}^{zz}\equiv 1/m_{\perp\mathrm{hh}}^*$ is given by Eqs. (16), $\gamma_{\mathrm{hh}}^{xx}$, $\gamma_{\mathrm{hh}}^{xy}$, and $\gamma_{\mathrm{hh}}^{yy}$ are given by Eq. (22), and where $\gamma_{\mathrm{hh}}^{xz}$ and $\gamma_{\mathrm{hh}}^{yz}$ are given by

$$\gamma_{\mathrm{hh}}^{xz}=6(\gamma_2-\gamma_3)d_{\mathrm{hh}}^{xz} \qquad \gamma_{\mathrm{hh}}^{yz}=6(\gamma_2-\gamma_3)d_{\mathrm{hh}}^{yz} \tag{C2}$$

with

$$d_{\mathrm{hh}}^{xz}=c_1^3c_3[h^4l^3+k^4l^3-(h^2+k^2)^3l]+2c_1c_2^2c_3h^2k^2l,$$

$$d_{\rm hh}^{yz}=c_1^2c_2c_3(hk^3-h^3k)l+c_2^3c_3(h^3k-hk^3). \quad \text{(C3)}$$

Then one can show that the in-plane effective mass in the in-plane direction $\hat{\mathbf{n}}=(n_1,n_2,0)$ (where $n_1^2+n_2^2=1$) in the limit of infinite barriers is given by

$$m^*_{\|\rm hh}(\mathbf{n})=[n_1^2\hat{\gamma}_{\rm hh}^{xx}+2n_1n_2\hat{\gamma}_{\rm hh}^{xy}+n_2^2\hat{\gamma}_{\rm hh}^{yy}]^{-1}, \quad \text{(C4)}$$

where

$$\hat{\gamma}_{\rm hh}^{xx}=\gamma_{\rm hh}^{xx}-\frac{(\gamma_{\rm hh}^{xz})^2}{4\gamma_{\rm hh}^{zz}},$$

$$\hat{\gamma}_{\rm hh}^{xy}=\gamma_{\rm hh}^{xy}-\frac{\gamma_{\rm hh}^{xz}\gamma_{\rm hh}^{yz}}{4\gamma_{\rm hh}^{zz}},$$

$$\hat{\gamma}_{\rm hh}^{xx}=\gamma_{\rm hh}^{xx}-\frac{(\gamma_{\rm hh}^{yz})^2}{4\gamma_{\rm hh}^{zz}}. \quad \text{(C5)}$$

Usually, $\gamma_{\rm hh}^{xz}$ and $\gamma_{\rm hh}^{yz}$ are small (proportional to $\gamma_2-\gamma_3$) relative to $\gamma_{\rm hh}^{zz}$, so that the contribution of the second terms in Eq. (C5) to the effective mass is small. Similar expressions can be derived for the lh subbands.

[1] G.C. Osbourn, J. Appl. Phys. **53**, 1586 (1982); J. Vac. Sci. Technol. **A 3**, 826 (1986).
[2] A.R. Adams, Electron. Lett. **22**, 249 (1986).
[3] A. Ghiti and U. Ekenberg, Semicond. Sci. Technol. **9**, 1575 (1994).
[4] M. Henini, P.J. Rodgers, P.A. Crump, B.L. Gallagher, and G. Hill, Appl. Phys. Lett. **65**, 2054 (1994).
[5] R. Notzel, N.N. Ledentsov, L. Daweritz, and K. Ploog, Phys. Rev. B **45**, 3507 (1992).
[6] J.B. Xia, Phys. Rev. B **43**, 9856 (1991).
[7] A.T. Meney, Superlatt. Microstr. **11**, 387 (1992).
[8] A. Ghiti, W. Batty, and E.P. O'Reilly, Superlatt. Microstr. **7**, 353 (1990).
[9] T. Hayakawa, T. Suyama, K. Takahashi, M. Kondo, S. Yamamoto, and T. Hijikata, J. Appl. Phys. **64**, 297 (1988).
[10] W.I. Wang, Surf. Sci. **174**, 31 (1986).
[11] S. Subbanna, H. Kroemer, and J.L Merz, J. Appl. Phys. **59**, 488 (1986).
[12] T. Fukunaga, T. Takamori, and H. Nakashima, J. Cryst. Growth **81**, 85 (1987).
[13] L.W. Molenkamp, R. Eppenga, G.W. 't Hooft, P. Dawson, C.T. Foxon, and K.J. Moore, Phys. Rev. B **38**, 4314 (1988).
[14] B.V. Shanabrook, O.J. Glembocki, D.A. Broido, and W.J. Wang, Phys. Rev. **B 39**, 13 533 (1989).
[15] K. Tsutsui, H. Mizukami, O. Ishiyama, S. Nakamura, and S. Furukawa, Jpn. J. Appl. Phys. **29**, 468 (1990).
[16] M. Lopez, T. Ikei, Y. Takano, K. Pak, and H. Yonezu, Jpn. J. Appl. Phys. **29**, 551 (1990).
[17] O. Brandt, K. Kanamoto, Y. Tokuda, N. Tsukada, O. Wada, and J. Tanimura, Phys. Rev. B **48**, 17 599 (1993).
[18] P.O. Vaccaro, M. Takahashi, K. Fujita, and T. Watanabe, Jpn. J. Appl. Phys. **34**, L **13** (1995).
[19] J.M. Luttinger and W. Kohn, Phys. Rev. **97**, 869 (1955).
[20] S.R. White and L.J. Sham, Phys. Rev. Lett. **47**, 879 (1981).
[21] G. Bastard, Phys. Rev. B **25**, 7584 (1982).
[22] E.C. Valadares, Phys. Rev. B **46**, 3935 (1992).
[23] D.L. Smith and C. Mailhiot, Rev. Mod. Phys. **62**, 1 (1990).
[24] L. De Caro and L. Tapfer, Phys. Rev. B **51**, 4374 (1995).
[25] E.O. Kane, *Handbook on Semiconductors* (North-Holland, New York, 1982), Vol. I, p. 193.
[26] R. Eppenga, M.F.H. Schuurmans, and S. Colak, Phys. Rev. B **36**, 1554 (1987).
[27] E.O. Kane, J. Phys. Chem. Solids **1**, 82 (1956).
[28] G. Bastard, *Wave Mechanics Applied to Semiconductor Heterostructures* (Les Editions de Physique, Les Ulis Cedex, 1988).
[29] D.E. Aspes and M. Cardona, Phys. Rev. B **17**, 726 (1978).
[30] G.L. Bir and G.E. Pikus, *Symmetry and Strain-Induced Effects in Semiconductors* (Wiley, New York, 1974).
[31] J.F. Nye, *Physical Properties of Crystals. Their Representation by Tensors and Matrices* (Oxford University Press, New York, 1985).
[32] G. Arlt and P. Quadflieg, Phys. Status Solidi **25**, 323 (1968).
[33] J.K. Cullum and R.A. Willoughby, *Lanczos Algorithms for Large Symmetric Eigenvalue Computation* (Birkhäuser, Boston, 1985).
[34] S.L. Wong, Phys. Rev. B **48**, 17 885 (1993).
[35] *Semiconductors: Physics of Group IV Elements and III-V Compounds*, edited by O. Madelung, M. Schulz, and H. Weiss, Landolt-Börnstein Group III. Vol. 17, Pt. a (Springer-Verlag, Berlin, 1982).
[36] S. Adachi, INSPEC Publ. No. (IEE), London, 1993, p. 16.
[37] C.G. van de Walle, Phys. Rev. B **39**, 1871 (1989).
[38] S. Baroni, R. Resta, A. Baldereschi, and M. Peressi, in *Spectroscopy of Semiconductor Microstructures*, edited by G. Fasol, A. Fasolino, and P. Lugli (Plenum Press, New York, 1989), p. 251.
[39] C. Ohler, R. Koleick, A. Förster, and H. Lüth, Phys. Rev. B **50**, 7833 (1994).
[40] D. Sun, E. Towe, P.H. Ostdiek, J.W. Grantham, and G.J. Vansuch, J. Select. Top. Quantum Electron. **1**, 674 (1995).
[41] B.K. Laurich, Phys. Rev. Lett. **61**, 649 (1989).
[42] K.J. Moore, P. Boring, B. Gil, and K. Woodbridge, Phys. Rev. B **48**, 18 011 (1993).
[43] M. Altarelli, Phys. Rev. B **28**, 842 (1983).
[44] M.G. Burt, J. Phys. Condens. Matter **4**, 6651 (1992).
[45] B.A. Foreman, Phys. Rev. B **48**, 4964 (1993); **49**, 1757 (1994).
[46] A.T. Meney, B. Gonul, and E.P. O'Reilly, Phys. Rev. B **50**, 10 893 (1994).